This is a copy of the published version, or version of record, available on the publisher's website. This version does not track changes, errata, or withdrawals on the publisher's site.

Valence shell photoelectron angular distributions and vibrationally resolved spectra of imidazole: A combined experimental–theoretical study

M. Patanen, A. R. Abid, S. T. Pratt, A. Kivimäki, A. B. Trofimov, A. D. Skitnevskaya, E. K. Grigoricheva, E. V. Gromov, I. Powis, and D. M. P. Holland

Published version information

Citation: M Patanen et al. Valence shell photoelectron angular distributions and vibrationally resolved spectra of imidazole: A combined experimental–theoretical study. J Chem Phys 155, no. 5 (2021): 054304

DOI: 10.1063/5.0058983

This article may be downloaded for personal use only. Any other use requires prior permission of the author and AIP Publishing.

This version is made available in accordance with publisher policies. Please cite only the published version using the reference above. This is the citation assigned by the publisher at the time of issuing the APV. Please check the publisher's website for any updates.

This item was retrieved from **ePubs**, the Open Access archive of the Science and Technology Facilities Council, UK. Please contact epublications@stfc.ac.uk or go to http://epubs.stfc.ac.uk/ for further information and policies.

The Journal of Chemical Physics

Valence shell photoelectron angular distributions and vibrationally resolved spectra of imidazole: A combined experimental–theoretical study

Cite as: J. Chem. Phys. **155**, 054304 (2021); https://doi.org/10.1063/5.0058983
Submitted: 04 June 2021 . Accepted: 09 July 2021 . Published Online: 04 August 2021

M. Patanen, A. R. Abid, S. T. Pratt, A. Kivimäki, A. B. Trofimov, A. D. Skitnevskaya, E. K. Grigoricheva, E. V. Gromov, I. Powis, D. M. P. Holland, et al.

View Online Export Citation CrossMark

ARTICLES YOU MAY BE INTERESTED IN

Modeling radiative and non-radiative pathways at both the Franck–Condon and Herzberg–Teller approximation level
The Journal of Chemical Physics **155**, 054108 (2021); https://doi.org/10.1063/5.0058643

Vibronic coupling in energy transfer dynamics and two-dimensional electronic–vibrational spectra
The Journal of Chemical Physics **155**, 054201 (2021); https://doi.org/10.1063/5.0056477

Software for the frontiers of quantum chemistry: An overview of developments in the Q-Chem 5 package
The Journal of Chemical Physics **155**, 084801 (2021); https://doi.org/10.1063/5.0055522

Challenge us.
What are your needs for periodic signal detection?
Watch

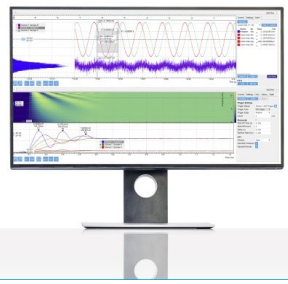

Zurich Instruments

AIP Publishing

© 2021 Author(s).

The Journal of Chemical Physics ARTICLE scitation.org/journal/jcp

Valence shell photoelectron angular distributions and vibrationally resolved spectra of imidazole: A combined experimental–theoretical study

Cite as: J. Chem. Phys. 155, 054304 (2021); doi: 10.1063/5.0058983
Submitted: 4 June 2021 • Accepted: 9 July 2021 •
Published Online: 4 August 2021

View Online Export Citation CrossMark

M. Patanen,[1] A. R. Abid,[1,2] S. T. Pratt,[3] A. Kivimäki,[1,4] A. B. Trofimov,[5,6] A. D. Skitnevskaya,[5] E. K. Grigoricheva,[5] E. V. Gromov,[5,7] I. Powis,[8] and D. M. P. Holland[9,a)]

AFFILIATIONS

[1] Nano and Molecular Systems Research Unit, Faculty of Science, University of Oulu, P. O. Box 3000, 90014 Oulu, Finland
[2] Molecular and Condensed Matter Physics, Uppsala University, Ångströmlaboratoriet, 752 37 Uppsala, Sweden
[3] Chemical Sciences and Engineering Division, Argonne National Laboratory, Lemont, Illinois 60439, USA
[4] MAX IV Laboratory, Lund University, P. O. Box 118, 22100 Lund, Sweden
[5] Laboratory of Quantum Chemical Modeling of Molecular Systems, Irkutsk State University, Karl Marx Str. 1, 664003 Irkutsk, Russia
[6] Favorsky's Institute of Chemistry, SB RAS, Favorsky Str. 1, 664033 Irkutsk, Russia
[7] Max-Planck Institute for Medical Research, Jahnstraβe 29, 69120 Heidelberg, Germany
[8] School of Chemistry, The University of Nottingham, University Park, Nottingham NG7 2RD, United Kingdom
[9] Daresbury Laboratory, Daresbury, Warrington, Cheshire WA4 4AD, United Kingdom

[a)] **Author to whom correspondence should be addressed:** david.holland@stfc.ac.uk

ABSTRACT

Linearly polarized synchrotron radiation has been used to record polarization dependent valence shell photoelectron spectra of imidazole in the photon energy range 21–100 eV. These have allowed the photoelectron angular distributions, as characterized by the anisotropy parameter β, and the electronic state intensity branching ratios to be determined. Complementing these experimental data, theoretical photoionization partial cross sections and β-parameters have been calculated for the outer valence shell orbitals. The assignment of the structure appearing in the experimental photoelectron spectra has been guided by vertical ionization energies and spectral intensities calculated by various theoretical methods that incorporate electron correlation and orbital relaxation. Strong orbital relaxation effects have been found for the 15a′, nitrogen lone-pair orbital. The calculations also predict that configuration mixing leads to the formation of several low-lying satellite states. The vibrational structure associated with ionization out of a particular orbital has been simulated within the Franck–Condon model using harmonic vibrational modes. The adiabatic approximation appears to be valid for the $X\ ^2A''$ state, with the β-parameter for this state being independent of the level of vibrational excitation. However, for all the other outer valence ionic states, a disparity occurs between the observed and the simulated vibrational structure, and the measured β-parameters are at variance with the behavior expected at the level of the Franck–Condon approximation. These inconsistencies suggest that the excited electronic states may be interacting vibronically such that the nuclear dynamics occur over coupled potential energy surfaces.

Published under an exclusive license by AIP Publishing. https://doi.org/10.1063/5.0058983

I. INTRODUCTION

Time-resolved, pump–probe photoelectron studies on imidazole ($C_3H_4N_2$) have played a prominent role in the investigation of the decay of $^1n\sigma^*$, $^1\pi\sigma^*$, and $^1\pi\pi^*$ excited states in heteroaromatic molecules.[1–4] Recently, Arbelo-González *et al.*[5] selected imidazole to test their newly developed semiclassical method of simulating steady state and time-resolved photoelectron spectra. This modeling allowed the time-dependent profile of a photoelectron band associated with a particular electronic state to be simulated. However, despite the extensive use of imidazole in time-resolved pump–probe investigations of excited state dynamics, the steady state valence shell photoelectron spectrum remains poorly characterized, with the only published spectra[6–8] being measured in the 1970s. These spectra were recorded using HeI radiation as the photon source, and hence were limited to photoelectron bands due to ionization out of the outer valence orbitals.

Imidazole has a planar (C_s) five-membered heteroaromatic ring structure, and its ground state valence shell electronic configuration, at the Hartree–Fock (HF) level of theory, may be given as follows:

Inner valence:

$(1a')^2$ through to $(10a')^2$.

Outer valence:

$(11a')^2\ (12a')^2\ (13a')^2\ (1a'')^2\ (14a')^2\ (15a')^2\ (2a'')^2\ (3a'')^2$.

This structure is visually depicted by plots of the outer valence orbitals (Fig. 1), and a more quantitative corroborating description can be obtained from a Mulliken atomic population analysis (see Table S1 of the supplementary material). Imidazole's π-electron system is formed by a single p_z electron from each of the C atoms, by a single p_z electron of the N_3 atom, and by the lone-pair of the N_1 atom. This gives rise to five π-type molecular orbitals, three of which ($1a''$, $2a''$, and $3a''$) are doubly occupied in the neutral ground state. The system of σ-orbitals includes the non-bonding $15a'$ orbital, which can be considered as a σ-type lone-pair (σ_{NLP}) on the N_3 atom. This σ_{NLP} orbital of imidazole is analogous to the corresponding orbital of pyridine and possesses rather similar shape and localization properties.[9,10]

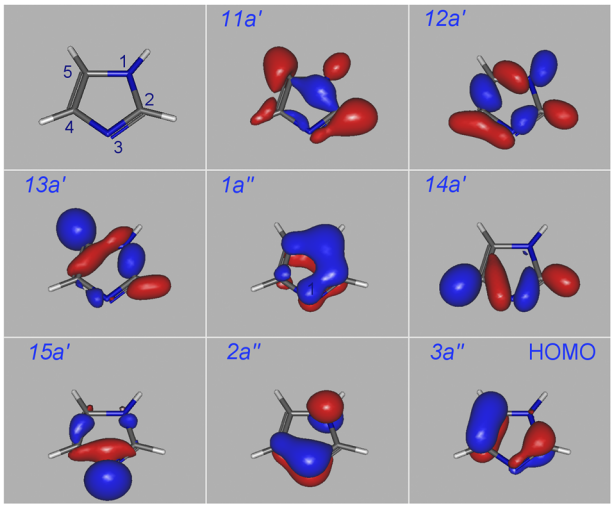

FIG. 1. The outer valence molecular orbitals of imidazole (iso-surface HF density plots). The top left panel indicates the molecular orientation used for these plots and the atomic numbering. The nitrogen, carbon, and hydrogen atoms are coded blue, gray, and white, respectively.

The aim of the present work is to study, both experimentally and theoretically, the electronic structure of the complete valence shell of imidazole and to investigate the photoionization dynamics. Linearly polarized synchrotron radiation has been used to record high resolution, polarization-dependent, photoelectron spectra of the outer valence orbitals in the photon energy range 21–100 eV. These have allowed the photoelectron angular distributions, as characterized by the anisotropy parameter β, and the electronic state intensity branching ratios (proportional to the photoionization partial cross sections) to be evaluated. Vibrational structure was observed in several of the photoelectron bands. In addition, the upper binding energy limit of the photoelectron spectrum recorded at a photon energy of 80 eV was extended to 40 eV to span the inner valence shell region.

The photoelectron bands appearing in the outer valence region of the experimental spectra have been assigned using vertical ionization energies calculated with the outer valence Green's function (OVGF) method,[11–13] the equation-of-motion coupled cluster approach at the level of the singles and doubles model (EOM-IP-CCSD),[14–18] and the linear response coupled cluster method accounting for single, double, and triple excitation (CC3).[19–22] A theoretical ionization spectrum of the complete valence shell was generated using the ionization energies and the associated relative spectral intensities, obtained with the third-order algebraic-diagrammatic construction scheme [ADC(3)] for the one-particle Green's function.[11,23–29] The ADC(3) results are applicable in regions of the spectrum where the single-electron picture of ionization breaks down,[30] and are essential in the assignment of the broad photoelectron bands observed in the inner valence region of imidazole.

The photoionization dynamics of the outer valence orbitals have been investigated theoretically by employing the Continuum Multiple Scattering–Xα (CMS–Xα) approach[31,32] to calculate photoelectron anisotropy parameters and photoionization partial cross sections.

Photoionization is often considered within the Born–Oppenheimer approximation,[33] in which the electronic and nuclear motions are separated, and the nuclei move over potential energy surfaces formed by the electrons. Each electronic state has an associated isolated potential energy surface. Under these conditions, the vibrational structure in a specific photoelectron band may be simulated by using the Franck–Condon (FC) factors connecting the initial neutral and the final ionic states.[34] Such vibrational structure will mainly consist of regular progressions involving excitation of the totally symmetric modes. Vibronic coupling, namely the interaction of two or more energetically close-lying electronic states through the nuclear motion, results in a breakdown of the Born–Oppenheimer approximation. The ensuing non-adiabatic dynamics can result in complex vibrational structure and in the excitation of non-totally symmetric vibrational modes. In the present work, the vibrational progressions in some of the outer valence photoelectron bands have been simulated in model calculations, employing the Born–Oppenheimer and Franck–Condon approximations, and compared to the observed

Published under an exclusive license by AIP Publishing

structure. Differences between the predicted and measured vibrational progressions may serve as an indicator of possible vibronic interaction.

II. EXPERIMENTAL APPARATUS AND PROCEDURE

The photoelectron spectra of imidazole were recorded on the gas phase end station[35] of the soft x-ray undulator-based FinEstBeAMS beamline[36] on the 1.5 GeV storage ring at MAX IV Laboratory.

Synchrotron radiation for the FinEstBeAMS beamline is produced by using an elliptically polarizing undulator (APPLE-II-type design[37]) that allows the radiation at the experiment to be either linearly or circularly polarized. A toroidal mirror collimates the beam emitted by the undulator prior to the radiation entering a plane grating monochromator.[38] The monochromator contains a 600 lines/mm grating and a 92 lines/mm grating. Another toroidal mirror focusses the dispersed radiation onto the monochromator exit slit, after which an ellipsoidal mirror refocusses the monochromatic radiation into the experimental chamber. The accessible photon energy range extends from 4.5 to 1300 eV.

The photoelectron spectra were recorded using a VG Scienta R4000 spectrometer, mounted in a fixed position, with the electron detection axis lying parallel to the plane of the electron orbit in the storage ring. The photoelectron spectra measured at photon energies between 21 and 55 eV were recorded using an analyzer pass energy of 10 eV and a 0.8 mm curved entrance slit, resulting in a theoretical spectrometer resolution of 20 meV. For photon energies between 60 and 100 eV, the analyzer pass energy was increased to 20 eV, leading to a resolution of 40 meV.

The 92 lines/mm grating was used, together with a monochromator exit slit width of 100 μm, for the spectra recorded at photon energies of up to 55 eV. The resulting theoretical optical resolution varies between 9 meV at 21 eV and 35 meV at 55 eV. The 600 lines/mm grating was employed, together with a monochromator exit slit width of 130 μm, for the spectra recorded at higher energies. The resulting theoretical optical resolution varies between 19 meV at 60 eV and 41 meV at 100 eV.

Translational Doppler broadening, associated with the thermal motion of the sample molecules, also contributes to the overall observed peak width.[39] For electrons ejected with kinetic energies of ~12.2 and 91.2 eV, corresponding to the formation of the $X\ ^2A''$ state in the vibrationally unexcited level at photon energies of 21 and 100 eV, the translational broadening amounts to ~5.2 and 14.3 meV, respectively.

The overall experimental resolution for the vibrationally unexcited level of the $X\ ^2A''$ state, due to contributions from the electron spectrometer, the photon bandwidth, and the Doppler broadening, varied between ~23 and 59 meV at photon energies of 21 and 100 eV, respectively.

The sample of imidazole (purchased from Sigma-Aldrich with a stated purity of >99%) was placed in a stainless steel crucible inside a resistively heated oven. This assembly was positioned directly below the interaction region, from which the electron lens of the Scienta spectrometer accepts electrons produced by photoionization. In practice, it was found that the vapor pressure of imidazole at room temperature was sufficient to allow a good quality photoelectron spectrum to be recorded in a reasonable accumulation time, so that additional heating was not required.

At each photon energy, photoelectron spectra were recorded with the electric vector of the linearly polarized incident radiation lying either parallel (θ = 0°) or perpendicular (θ = 90°) to the Scienta analyzer's electron acceptance axis. The orientation of the polarization could be changed by altering the settings of the undulator. Assuming electric dipole photoionization by completely linearly polarized radiation, the differential photoionization partial cross section can be expressed as[40]

$$\frac{d\sigma}{d\Omega} = \frac{\sigma}{4\pi}[1 + \beta P_2(\cos\theta)], \tag{1}$$

where σ is the angle-integrated partial cross section, $d\Omega$ is the differential solid angle element in the direction specified by the polar angle θ, β is the photoelectron anisotropy parameter, $P_2(\cos\theta)$ is the Legendre polynomial of second order, and θ is the electron ejection angle relative to the polarization axis. Equation (1) can be rearranged into the more convenient form as follows:[41,42]

$$\beta = \frac{2(I_0 - I_{90})}{I_0 + 2I_{90}}, \tag{2}$$

where I_0 and I_{90} are the normalized electron intensities for parallel and perpendicular polarization orientations relative to the electron detector axis, respectively. All the spectra were normalized to the sample pressure, the accumulation time, and the photon flux prior to processing. Some of the spectra shown in this paper are so-called magic angle spectra (θ = 54.7°), where the electron intensity is independent of the photoelectron anisotropy parameter. Such magic angle spectra are synthesized from the spectra measured at θ = 0° and θ = 90° using the following expression:[41,42]

$$I_{MA} = \frac{(I_0 + 2I_{90})}{3}. \tag{3}$$

The binding energy scale of each photoelectron spectrum was calibrated using the H_2O^+ $X\ ^2B_1$ state ionization energy (IE) of 12.622 eV.[43] A small signal due to water was present in most of the spectra of imidazole.

Prior to our measurements on imidazole, the performance of the electron spectrometer was checked by recording polarization dependent photoelectron spectra encompassing the Xe $5p^5\ ^2P_{1/2}$ and $^2P_{3/2}$ states over the same photon energy range used for our experiment on imidazole. The β-parameters derived from these spectra were in accord with the well-established values.[44–46] These spectra also allowed the transmission efficiency of the electron analyzer as a function of electron kinetic energy to be determined, using the following procedure. The relative photoionization partial cross section of the Xe 5p orbital was determined from our synthesized magic angle spectra, while also taking into account the incident photon flux at each photon energy. This relative Xe 5p photoionization partial cross section was then compared with the absolute photoionization partial cross section,[47,48] thereby allowing the transmission efficiency to be deduced. All our photoelectron spectra of imidazole were normalized to the derived transmission efficiency.

The experimental photoelectron anisotropy parameter and branching ratio associated with a particular binding energy range were determined as described by Powis *et al.*[41] Table I lists the

Published under an exclusive license by AIP Publishing

TABLE I. Energy ranges used to analyze the experimental photoelectron spectra.

Region	Energy range (eV)	Orbitals[a]
1	8.60–9.70	3a″
2	9.75–10.50	15a′, 2a″
3	10.50–11.30	15a′, 2a″
4	13.10–13.70	1a″, 14a′
5	13.70–14.30	14a′, 1a″
6	14.30–15.10	1a″, 13a′, 12a′
7	15.10–16.30	13a′, 12a′
8	17.30–18.30	11a′, 10a′, 9a′
9	18.30–18.90	11a′, 10a′, 9a′
10	18.90–19.60	11a′, 10a′, 9a′
11	19.60–21.00	11a′, 10a′, 9a′

[a]Orbitals possibly contributing to the observed electron intensity in a specific energy range.

energy ranges used to analyze the photoelectron spectra of imidazole. Within each range, a mean β-parameter is evaluated by summing the electron counts in the normalized parallel and perpendicular polarization dependent spectra and inserting these summed intensities into Eq. (2). The intensities required for the branching ratios are evaluated in a similar manner. These mean β-parameters and branching ratios are thus vibrationally averaged values and can be compared with the corresponding theoretical predictions obtained from our fixed nuclei, CMS–Xα calculations. Our analysis procedure also allows the variation in the β-parameter as a function of the binding energy across a specific photoelectron band to be determined. This capability enables any dependence of the β-parameter on the level of vibrational excitation to be examined. The potential errors in the β-parameters and branching ratios were estimated by propagation of the assumed statistical counting uncertainty through the evaluation of Eq. (2). The resulting error bars do not include any uncertainty associated with possible systematic errors that may arise, for example, from non-ideal performance of the spectrometer or photon delivery system.

III. COMPUTATIONAL DETAILS

A. Vertical ionization energies

The vertical ionization energies of imidazole and the corresponding relative spectral intensities (pole strengths, P) for transitions belonging to the outer valence region were computed using several methods, including the HF theory at the level of Koopmans' theorem, the OVGF method,[11–13] the third-order non-Dyson algebraic-diagrammatic construction (ADC) method [IP-ADC(3)],[23–26] the third-order Dyson ADC method [ADC(3)],[11,27–29] the equation-of-motion coupled-cluster (CC) theory for ionization potentials at the level of singles and doubles model (EOM-IP-CCSD),[14–18] and the CC3 method[19–22] in combination with the continuum orbital approach.[49] A cc-pVTZ basis set[50,51] was used in all cases [with the exception, discussed below, of the Dyson ADC(3) calculations], and the K-shell orbitals were kept frozen. Additionally, the EOM-IP-CCSD calculations were repeated using a series of the cc-pVnZ and aug-cc-pVmZ basis sets of improving quality (n = D, T, Q, 5; m = D, T, Q),[50,51] thereby allowing the ionization energies to be extrapolated to the complete basis set (CBS) limit.[52,53] The OVGF and CC3 calculations were performed using the Gaussian[54] and CFOUR[55] programs, respectively, whereas the Q-Chem[56] program was employed for the IP-ADC(3) and EOM-IP-CCSD calculations.

The theoretical spectral envelope for the valence shell ionization of imidazole up to 40 eV was generated using the results of the IP-ADC(3) and Dyson ADC(3) calculations. Both methods provide an equivalent third-order description of the ionization spectrum. Whereas IP-ADC(3) is, in general, computationally very efficient, its recent implementation[25,26] still lacks a block-Lanczos diagonalization procedure. Such a procedure is crucial for the generation of the spectral envelope at energies higher than those of the outer valence region where the single electron picture of ionization breaks down[30] and many eigenstates have to be computed. In order to recover this part of the spectrum (~23 to 40 eV), we resorted to the older Dyson ADC(3) scheme that allows block-Lanczos calculations to be carried out, and which has proven successful in previous studies.[9,10,57,58] However, owing to the shortcomings of this older Dyson ADC(3) implementation, a smaller basis set, consisting of the cc-pVTZ basis on the second row atoms and the cc-pVDZ basis[50,51] on the hydrogens, had to be used (the Cartesian representation of the d-functions was employed). This, however, is not expected to influence the resulting theoretical spectral profile which was constructed by convoluting the combined IP-ADC(3)/Dyson ADC(3) spectrum with Gaussians of 0.55 eV FWHM (full width at half maximum). The Dyson ADC(3) calculations were performed using the original code linked to the local version of the Gamess *ab initio* program package.[59,60]

The calculations of the vertical ionization spectra were performed using the equilibrium ground state geometrical parameters obtained by a full geometry optimization at the level of the second-order Møller–Plesset (MP2) perturbation theory (PT) in combination with the cc-pVTZ basis sets. The Gaussian package of programs was used in the calculations.[54] The computed geometrical parameters are presented in Table S2 and compared with the available experimental data.

B. Franck–Condon simulations of vibrational spectra

Franck–Condon (FC) simulations were prepared using harmonic vibrational frequencies and normal modes. The numbering of the vibrational modes follows the nomenclature recommended by Herzberg.[61] The harmonic vibrational analysis required for the ground state neutral and cation used B3LYP/cc-pVTZ calculations. For the excited cation states, we used time-dependent density functional theory with the B3LYP functional (TD-B3LYP) and cc-pVXZ (X = D, T) bases. Franck–Condon factors were then calculated using the adiabatic hessian model, including Duschinsky rotations, provided in Gaussian 16,[62] and convoluted with a 75 cm^{-1} FWHM Gaussian shaping function to generate realistic spectral profiles.

C. CMS-Xα calculations of photoionization properties

Photoionization properties (cross sections, β-parameters) were calculated at the same fixed, initial geometry using a static-exchange independent electron, continuum multiple scattering model[31,32] with a Xα exchange potential (CMS–Xα). Our method has been described previously[63,64] and is only briefly summarized here. The

Published under an exclusive license by AIP Publishing

neutral molecule potential is modeled as overlapping spherical regions centered on each atomic site, with the whole molecule enclosed within a spherically symmetric outer sphere that extends to infinity. Within each spherical region the exchange contribution to an effective one-electron potential is represented using the Slater Xα local density approximation.[65] The wavefunctions are expressed in a symmetry-adapted basis of spherical harmonic functions on each center, with radial functions obtained by direct numerical integration within the spherical zones of the potential, and the trial potential is then iterated to self-consistency. One electron continuum functions are found by solving the scattering problem with this potential after its adaptation to ensure the correct asymptotic Coulombic behavior for the electron–ion system. Electric dipole photoionization matrix elements and hence cross sections and β-parameters may then be calculated. The calculations were performed using the MP2/cc-pVTZ optimized geometry with atomic sphere dimensions set to 0.86 of the Norman radius.[66] Spherical harmonic angular basis functions ranging up to l_{max} = 5; 2; 1 were used in, respectively, the outer sphere, the first row atoms, and the H atoms. For the continuum calculations, l_{max} cutoffs were increased to 10; 6; 4.

IV. RESULTS AND DISCUSSION

A. Assessment of calculated binding energies

The various calculated outer valence vertical ionization energies are listed in Table II and compared to the experimental results obtained in the present work. A strict quantitative comparison between the theoretical and experimental results is, as usual, complicated by the fact that the measured positions of the spectral maxima are only approximately related to the vertical ionization energies, which are defined as the transition energies at the ground state equilibrium geometry. In addition, the position of the maximum in the experimental peak may sometimes appear displaced due to superposition with other neighboring states or hot band ionizations. All the theoretical methods treating electron correlation and orbital relaxation (i.e., all schemes except for the HF/Koopmans' theorem) yield rather consistent ionization energies, which agree with the experimental values. However, a closer inspection of the theoretical results reveals some differences that are discussed in more detail.

In the OVGF and ADC(3) methods, the one-hole (1*h*) ionization processes are treated through third order of the many-body perturbation theory (PT). The 1*h*-type states are described by these computational schemes in a similar manner so that the errors with respect to the experiment, as seen from Table II, have comparable magnitude and character.

In contrast to the OVGF approach, the ADC(3) schemes explicitly take into account configuration interaction between the (1*h*) and the two-hole-one-particle (2*h*-1*p*) cationic states, which are treated here consistently through third and first order of PT, respectively. The states with 2*h*-1*p* and mixed 1*h*/2*h*-1*p* character can therefore be qualitatively correctly reproduced in ADC(3), whereas the OVGF method fails in such situations. As can be seen from the ADC(3) pole strength values, *P*, (reflecting the 1*h* character of the final states), the 1*h*/2*h*-1*p* configuration mixing takes place in several low-lying cationic states of imidazole. In particular, the $(1a'')^{-1}$ and $(13a')^{-1}$ states are affected; these possess values, *P*, of ~0.5 and ~0.7, respectively (Table II). This implies that part of their intensity is transferred to 2*h*-1*p* satellites.

The lowest of these satellites ($^2A''$) with significant intensity ($P \approx 0.21$) is predicted, by the present calculations (Table II), as the fourth lowest state in the spectrum at 13.8/13.9 eV [depending on the ADC(3) variant being used]. The composition of this and the other $^2A''$ states gaining intensity from the 1a″ orbital is presented in Table III, where the composition is quantified in terms of the weights of the most important 1*h* and 2*h*-1*p* configurations,

TABLE II. Vertical ionization energies (eV) of the outer valence transitions in imidazole. These are computed using the HF/Koopmans, OVGF, IP-ADC(3), Dyson ADC(3), EOM-IP-CCSD, and CC3 methods. The best theoretical estimates (BTEs) and the experimental values are also listed. For the ADC(3) schemes, relative intensities (pole strengths) are presented in parentheses.[a]

State	MO		HF	OVGF	IP-ADC(3)		Dyson ADC(3)		CCSD	CC3	BTE[b]	Expt.[c]
$X\ ^2A''$	3a″	π	8.63	8.82	8.85	(0.90)	8.89	(0.89)	8.91	8.85	9.02	9.1
$A\ ^2A'$	15a′	nσ	11.85	10.27	10.47	(0.89)	10.56	(0.89)	10.15	10.08	10.30	10.4
$B\ ^2A''$	2a″	π	10.85	10.25	10.34	(0.87)	10.40	(0.87)	10.32	10.30	10.51	10.4
$^2A''$	1a″	π	⋯	⋯	13.78	(0.21)	13.90	(0.24)	⋯	13.94	⋯	13.8
$C\ ^2A'$	14a′	σ	15.45	14.16	14.32	(0.89)	14.34	(0.89)	14.18	14.06	14.25	13.8
$D\ ^2A''$	1a″	π	16.25	14.55	14.90	(0.50)	15.03	(0.46)	14.60	⋯	14.81	14.8–15.3
$E\ ^2A'$	13a′	σ	16.37	15.05	15.20	(0.76)	15.23	(0.71)	15.03	14.89	15.09	14.8–15.3
$^2A'$	13a′	σ	⋯	⋯	15.26	(0.14)	15.28	(0.20)	⋯	⋯	⋯	14.8–15.3
$F\ ^2A'$	12a′	σ	16.51	15.10	15.32	(0.87)	15.36	(0.88)	15.14	⋯	15.33	14.8–15.3
$G\ ^2A'$	11a′	σ	20.61	18.65	18.58	(0.57)	18.62	(0.59)	18.67	17.95	18.12	17.9

[a]The cc-pVTZ basis set was employed everywhere except for the Dyson ADC(3) calculations, which were performed using the cc-pVTZ basis on the second row atoms and the cc-pVDZ basis on the hydrogens.
[b]The best theoretical estimates were obtained by adding the CBS correction for the cc-pVTZ basis (Table IV) to the CC3 values. In the case of the $D\ ^2A''$ and $F\ ^2A'$ states where CC3 values could not be obtained, the correction is added to the EOM-IP-CCSD values.
[c]As derived from the band maxima in the photoelectron spectrum recorded with a photon energy of 80 eV. For the $X\ ^2A''$ state, an approximate position of the center of gravity for the band is given (which roughly corresponds to the vertical transition energy). The energy of the 0–0 transition is 8.842 eV.

Published under an exclusive license by AIP Publishing

TABLE III. Transitions originating from ionization of the 1a″ orbital of imidazole: vertical ionization energy (*IE*, eV); pole strength (*P*, a.u); weight (*C*, percent) of the most important 1*h* and 2*h*-1*p* configurations (specified) in the respective wavefunction, as calculated at the IP-ADC(3) level of theory; and their type.[a]

IE	*P*	*C* (1*h*)	*C* (2*h*-1*p*)	Type
13.78	0.21	20 $(1a'')^{-1}$	29 $(3a'')^{-2}(4a'')^{1}$	Shake-down
14.90	0.50	51 $(1a'')^{-1}$	7 $(3a'')^{-2}(4a'')^{1}$	Main line
15.36	0.02	1 $(1a'')^{-1}$	29 $(3a'')^{-2}(5a'')^{1}$	Shake-up
16.06	0.07	7 $(1a'')^{-1}$	17 $(2a'')^{-1}(3a'')^{-1}(4a'')^{1}$	Shake-up
17.70	0.06	5 $(1a'')^{-1}$	13 $(2a'')^{-1}(3a'')^{-1}(5a'')^{1}$	Shake-up
19.56	0.06	6 $(1a'')^{-1}$	13 $(2a'')^{-2}(4a'')^{1}$	Shake-up

[a]Only transitions with $P \geq 0.01$ are shown.

as computed at the IP-ADC(3) level of theory. As can be seen, the 1a″ orbital gives rise to a large number of ionization transitions, most of which can be referred to as various satellites. The largest $(1a'')^{-1}$ contribution, of 51%, is to the $^2A''$ state with a vertical ionization energy of 14.90 eV, which can be formally considered as the "main" state. The lowest satellite state at 13.8 eV can therefore be considered as a shake-down satellite,[67] whereas the remaining $^2A''$ states derived from the 1a″ orbital, lying above the main-line, represent shake-up satellites.[30,67] The situation where the innermost π orbital is involved in extensive satellite formation while its neighbors produce only distinct main ionization lines is typical for heterocyclic molecules.[9,68–70] Such selective breakdown effects for the innermost π orbital, in contrast to the more general picture of shake-up satellite formation, have been discussed in detail in relation to pyridine[9] and the halothiophenes.[68–70] As follows from the analysis of the interaction matrix elements,[68] the selective breakdown phenomena[71] originate from the specific localization properties of the innermost and vacant π orbitals and, more generally, from the strong electron correlation effects associated with the π orbital subsystem in heterocyclic molecules.

The next intense satellite ($^2A'$) is predicted at 15.3 eV. Further, although less intense 2*h*-1*p* states are identified that can contribute to the inner valence region at higher energy, but these are not included in Table II. As explained above, these satellite states are not recovered by the OVGF calculations.

A distinctly higher level of theory is provided by the CC3 scheme, which treats the 1*h* and 2*h*-1*p* states through third and second orders of PT, respectively. This scheme is the well-established benchmark method. Indeed, the present CC3 results agree very well with the experimental data. For three cases in Table II, the CC3 data are missing since the calculations did not converge to the correct state. The results of the second CC scheme employed in our study, EOM-IP-CCSD, are nearly as good as those obtained using the CC3 scheme, although the EOM-IP-CCSD scheme provides only second-order PT consistency for the 1*h*-type states and first-order consistency for the 2*h*-1*p* states.[23] The EOM-IP-CCSD and CC3 results disagree for the $(11a')^{-1}$ state, which possesses an increased 2*h*-1*p* character, where their disparity in ionization energies amounts to 0.7 eV.

Whereas the results of the CC and ADC(3) methods appear to be comparably accurate, there is an important distinction between them concerning the position of the $(15a')^{-1}$ state, associated with the σ_{NLP} nitrogen lone-pair orbital, in the spectrum. The ADC(3) methods predict the $(15a')^{-1}$ state to be the third lowest state, as also do the HF/Koopmans and OVGF calculations, while the CC methods shift it down in energy to become the second lowest state. This situation is very similar to that for the σ_{NLP} orbital in pyridine where the shift is caused by the large relaxation energy associated with the ionization out of this orbital.[9] In imidazole, the relaxation mechanism is essentially the same as in pyridine and consists in screening of the σ_{NLP} hole by the π–π^* excitations. The latter is recognized, e.g., from the notable admixtures of $(\sigma_{NLP})^{-1}(\pi)^{-1}\pi^*$-type configurations in the expansion of the ADC(3) eigenvectors for the $(15a')^{-1}$ state.

The relaxation energy can be estimated as a difference between the results of the HF/Koopmans and the HF/ΔSCF calculations (corresponding to the frozen- and relaxed-density HF pictures, respectively). In our HF/ΔSCF calculations, the cc-pVTZ basis set was employed and the cationic states were computed at the restricted open-shell HF (ROHF) level of theory. The resulting vertical ionization energies for the $(3a'')^{-1}$ and $(15a')^{-1}$ states are 7.63 and 8.95 eV, respectively, which implies relaxation shifts of 1.0 and 2.90 eV, respectively. This demonstrates that the relaxation energy for the σ_{NLP} orbital in imidazole is indeed very large and even exceeds the relaxation energy for the similar orbital in pyridine (2.73 eV).[9]

Since the energy gap between the $(15a')^{-1}$ and $(2a'')^{-1}$ states, which are interchanged in the spectrum, is rather small (≤0.2 eV in the correlated methods), their true order is, in fact, still questionable and represents a subtle issue. The existing accuracy estimates for the ADC(3) and CC methods,[26,72–74] however, indicate that the predictions of the CC3 scheme are likely to be more reliable. It is also important to note that they are supported by the results of the EOM-IP-CCSD method.

In order to further validate our findings, we studied the basis set dependence of the EOM-IP-CCSD ionization energies, extrapolating toward the CBS limit.[52,53] As can be seen from the results appearing in Table IV, the systematic increase in the basis set size up to aug-cc-pVQZ does not influence the order of the cationic states but incrementally improves all the ionization energies by an approximately uniform shift. The extrapolated CBS estimates differ from the cc-pVTZ values presented in Table II by about +0.2 eV. The present results indicate that the cc-pVTZ basis yields reasonably converged ionization energies, although it might be advantageous to augment the basis with the diffuse functions (aug-cc-pVTZ) since this brings the results distinctly closer to the CBS limit. The evaluated CBS corrections were added to the CC3/cc-pVTZ results to obtain the best theoretical estimates (BTEs) for the imidazole ionization energies (Table II). For the $D\ ^2A''$ and $F\ ^2A'$ states, where the CC3 results are missing, the EOM-IP-CCSD ionization energies were used instead.

B. Assignment of the photoelectron band structure

Figure 2(a) presents the complete inner and outer valence region photoelectron spectrum of imidazole recorded with a photon energy $h\nu$ = 80 eV, while beneath it [Fig. 2(b)] is shown, for comparison, a simulation derived from the ADC(3) calculated ionization energies, as discussed in Sec. III A. The simulation provides a very reasonable account of the experimentally observed spectral profile, including the extensive satellite structure seen above ~19 eV.

Published under an exclusive license by AIP Publishing

TABLE IV. Vertical ionization energies (eV) of imidazole computed using the EOM-IP-CCSD method and series of the cc-pV*n*Z and aug-cc-pV*m*Z basis sets (*n* = D, T, Q, 5; *m* = D, T, Q) as well as the estimates for the complete basis set limit, Δ(∞).

State	MO	cc-pVDZ	aug-cc-pVDZ	cc-pVTZ	aug-cc-pVTZ	cc-pVQZ	aug-cc-pVQZ	cc-pV5Z	Δ(∞)[a]
$X\,^2A''$	3a″	8.64	8.85	8.91	9.00	9.01	9.05	9.06	9.08
$A\,^2A'$	15a′	9.79	10.07	10.15	10.26	10.29	10.33	10.34	10.37
$B\,^2A''$	2a″	10.00	10.24	10.32	10.43	10.45	10.49	10.50	10.53
$C\,^2A'$	14a′	13.95	14.14	14.18	14.27	14.29	14.33	14.34	14.37
$D\,^2A''$	1a″	14.33	14.53	14.60	14.70	14.72	14.77	14.77	14.81
$E\,^2A'$	13a′	14.80	14.98	15.03	15.11	15.14	15.17	15.18	15.23
$F\,^2A'$	12a′	14.92	15.09	15.14	15.22	15.24	15.28	15.29	15.33
$G\,^2A'$	11a′	18.46	18.62	18.67	18.74	18.77	18.80	18.81	18.84

[a]Mean of the cc-pV*n*Z and aug-cc-pV*n*Z basis set limits ($n \to \infty$); see the text for details.

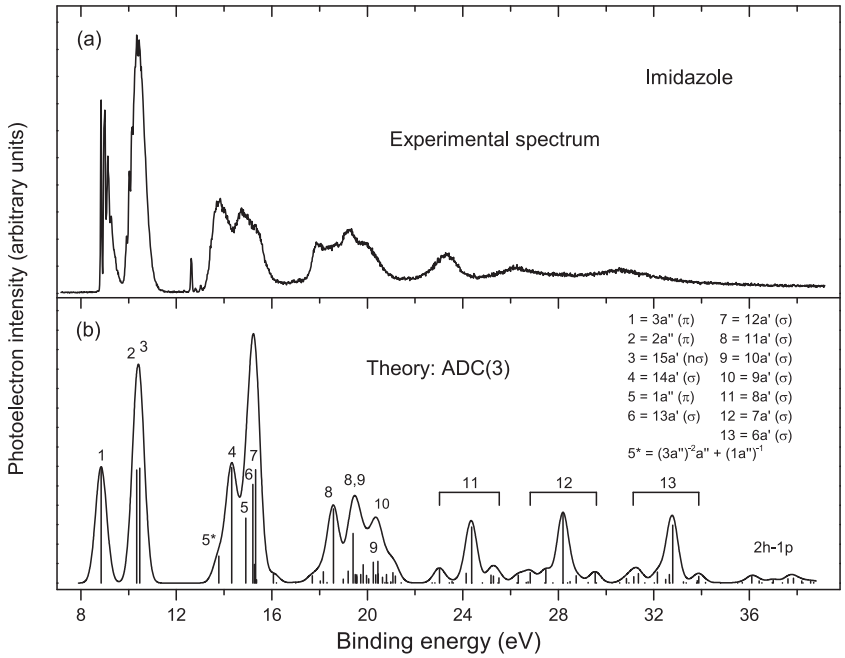

FIG. 2. The complete inner and outer valence region photoelectron spectrum of imidazole: (a) the experimental spectrum recorded with parallel linear polarization using a photon energy of 80 eV (the sharp feature seen at 12.62 eV binding energy is a residual trace of H_2O in the sample); (b) simulated spectral profile using ADC(3) calculated transition energies and pole strengths (Table II), convolved with a 0.55 eV FWHM Gaussian shaping function.

A more detailed example of the outer valence region of the photoelectron spectrum (PES), recorded with parallel and perpendicularly polarized radiation, is plotted in Fig. 3. The BTEs of the vertical binding energies (Table II), as discussed in Sec. IV A, are marked against the experimental band structure. This now informs our attempts to assign electronic structure to the photoelectron bands.

The first band displays extended vibrational progressions (Figs. 3 and 4). From the first peak in the experimental spectrum, at 8.842 eV, the vibrational structure extends up to ~9.7 eV, with an approximate center of gravity at 9.1 eV. This energy is very similar to the BTE value of 9.02 eV for ionization out of the 3a″(π) orbital, allowing an unambiguous assignment of this band. The second band, located between ~9.8 and 11.4 eV, also exhibits vibrational structure and has a maximum at ~10.4 eV (Fig. 3). According to our theoretical results, this band can be attributed to the 15a′(σ_{NLP}) and 2a″(π) orbitals, with the BTEs for their ionization energies being 10.30 and 10.51 eV, respectively. The mean of these two values matches the position of the observed band maximum.

Toward higher binding energy, the spectrum becomes increasingly complex and exhibits a broad, structured feature between ~13.2 and ~16 eV, with maxima at ~13.8 and ~14.8 eV, and a shoulder at ~15.3 eV (Figs. 2 and 3). Our calculations indicate that the maximum at 13.8 eV originates mainly from the 14a′(σ) orbital (Table II and Fig. 2). However, our BTE for the ionization energy of the 14a′(σ) orbital, 14.25 eV, is higher than the energy of the experimental maximum. A possible reason for this discrepancy is that the observed peak may originate from a superposition of several electronic/vibronic transitions. This view is supported by our ADC(3) calculations which predict an intense $^2A''$ 2*h*-1*p* satellite related to the 1a″(π) orbital in this energy region (see discussion above). The second maximum, at ~14.8 eV, corresponds, according to our theoretical results, to ionization out of the 1a″(π) orbital, whose BTE energy is 14.81 eV, while the shoulder at ~15.3 eV can be assigned

Published under an exclusive license by AIP Publishing

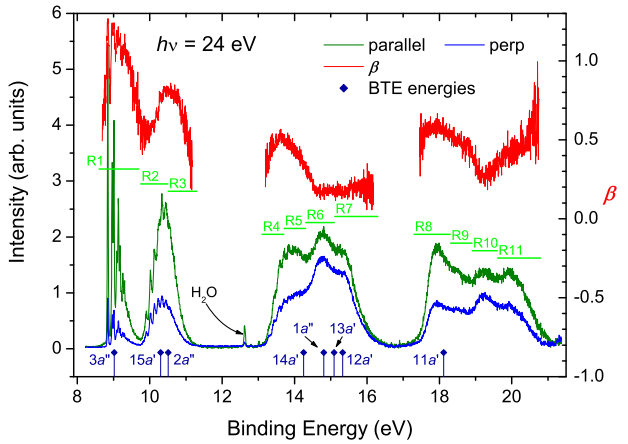

FIG. 3. An outer valence photoelectron spectrum of imidazole, recorded with a photon energy of 24 eV. Included here are normalized measurements made with the linear polarization axis set either parallel or perpendicular to the spectrometer detection axis, showing the different intensity distributions. The photoelectron anisotropy parameter β derived from these spectra, evaluated point by point across the spectrum, is also plotted. [The plotting of β is suppressed in regions of low photoelectron intensity since here the form of Eq. (2) greatly amplifies the statistical noise in the weak background baseline.] The green horizontal bars mark the regions (R1–R11) used to analyze the spectra. The binding energy ranges corresponding to these regions are listed in Table I. At the bottom are marked the best theoretical estimates (BTEs) obtained by applying the complete basis set extrapolation estimate to the CC3/cc-pVTZ calculations (Table IV).

to the 12a′(σ) orbital with a BTE energy of 15.33 eV. The 13a′(σ) orbital, characterized by a BTE energy of 15.09 eV, apparently also contributes to the shoulder, as also do various 2*h*-1*p* satellites, predicted here by our ADC(3) calculations (Table II and Fig. 2).

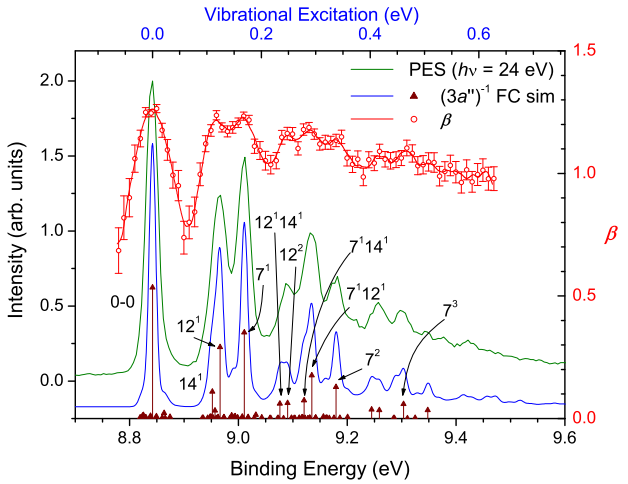

FIG. 4. The magic angle $X\ ^2A''$ state photoelectron spectrum of imidazole recorded using a photon energy of 24 eV. Also shown is a 300 K FC simulated spectrum with the calculated B3LYP/cc-pVTZ harmonic frequencies scaled by a factor of 0.97.[75] Its vibrationless origin is set at a binding energy of 8.842 eV. The intensity of both the experimental and the simulated spectra is arbitrarily scaled for plotting. Assignments of the most intense peaks in the stick spectrum are marked. Also shown is the β anisotropy parameter curve obtained across this band.

The high density of states, and their complex nature, make the spectral envelope observed in the energy range 13.2–16 eV difficult to reproduce, leading to the discrepancy between the ADC(3) and experimental spectral profiles (Fig. 2).

The next intense feature in the experimental photoelectron spectrum, located between 17.5 and 21 eV, contains three peaks at ~17.9, 19.2, and 19.9 eV (Figs. 2 and 3). Our results indicate that only the lowest of these peaks can be tentatively assigned to a distinct transition, namely, ionization out of the 11a′(σ) orbital with a BTE energy of 18.12 eV. The remaining higher-lying peaks are built from various satellites originating from the 11a′(σ), 10a′(σ), and 9a′(σ) orbitals (Fig. 2). The energy of ~19 eV therefore marks the onset of a more extensive breakdown in the single particle picture of ionization.[30]

Above this 19 eV binding energy, the ADC(3) calculation predicts that the spectrum will exclusively consist of various 2*h*-1*p* satellites which are related to the inner valence 8a′(σ), 7a′(σ), and 6a′(σ) orbitals. As can be seen from the spectrum in Fig. 2, the groups of satellites associated with the 8a′(σ), 7a′(σ), and 6a′(σ) orbitals can be assigned to the diffuse spectral features with maxima at 23.3, 26.1, and 30.6 eV, respectively.

C. Vibrational structure and Franck–Condon harmonic simulations

The experimental $(3a'')^{-1}$ $X\ ^2A''$ state photoelectron band is plotted in Fig. 4, together with a 300 K Franck–Condon harmonic vibrational simulation. The calculated harmonic frequencies are listed in Table S3 (supplementary material). The plotting offset of the internal vibrational energy scale of the simulation has been adjusted for the best alignment between the observed and the predicted vibrational structure. An expanded view of the first peak in Fig. 4 is presented in Fig. S1 (supplementary material). The FC simulation indicates that the peak maximum accurately coincides with the position of the 0–0 origin transition, with no skewing of the peak profile resulting from the adjacent, much less intense hot band transitions. Consequently, we identify the experimental peak maximum at 8.842 ± 0.001 eV with the adiabatic ionization energy.

Across the whole of this first band a very satisfactory agreement has been achieved between the experimental and simulated spectra, and this allows the vibrational structure to be assigned. The simulation indicates that the principal peaks are due to excitations involving the ν_7^+ and ν_{12}^+ modes, either alone or in various combinations with each other. In addition, smaller contributions arise from excitation of the ν_{14}^+ mode, either alone or in combination with the ν_7^+ or ν_{12}^+ modes. Figure S2 of the supplementary material shows the experimental $X\ ^2A''$ state photoelectron band with the main peaks marked and assigned; Table S4 lists the corresponding binding energies. Experimentally derived vibrational energies of 170 and 124 meV have been obtained for the ν_7^+ and ν_{12}^+ modes, respectively, based on the spacing between the peak due to the adiabatic transition and that associated with the first member in each progression. Our calculated energies for the ν_7^+ and ν_{12}^+ modes, after applying an appropriate harmonic scaling of 0.968,[75] are 170 and 125 meV, respectively.

The good agreement between the experimental and simulated spectra for the first photoelectron band indicates that the FC

Published under an exclusive license by AIP Publishing

model, including the Born–Oppenheimer approximation invoking separable nuclear and electronic motions, appears valid for the $X\,^2A''$ state.

The second photoelectron band, lying in the binding energy range ~9.8 to 11.4 eV, is shown in Fig. 5. Experimentally, this band exhibits vibrational structure, which appears to consist of a single progression, up to a binding energy of ~10.55 eV. Although the separation between the vibrational peaks is slightly irregular, the average spacing is ~108 meV. According to our BTEs [Table II and Fig. 5(a)], this band should arise from ionization out of the 15a′ and 2a″ orbitals, with the vertical binding energy of the 15a′ orbital being very slightly lower (0.21 eV) than that of the 2a″ orbital. However, some of the alternative calculations in Table II have the ordering exchanged. In any event, the predicted small differences between these orbital energies suggest that the associated vibrational envelopes are likely to overlap. Figures 5(b) and 5(c) compare the experimental spectrum with the FC simulated spectra due to the 15a′ and 2a″ orbitals. These simulated profiles include excitations from all thermally populated vibrational levels in the neutral molecule, while, for plotting, the underlying stick spectra have been restricted to the more intense transitions to avoid an excessively congested appearance. The principal vibrational assignments suggested by these simulations are marked in panels (b) and (c) of Fig. 5.

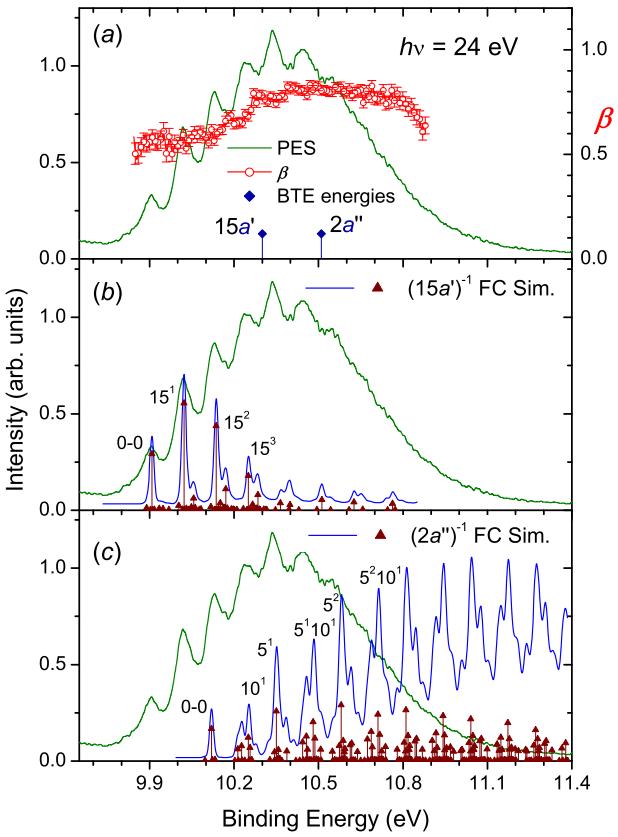

FIG. 5. The second band of the magic angle photoelectron spectrum of imidazole recorded with a photon energy of 24 eV: (a) the β-parameter derived from the parallel and perpendicular polarization recordings [Eq. (2)] and the BTE values for the vertical 15a′ and 2a″ ionizations, (b) comparison with TD-B3LYP/cc-pVDZ FC simulation for 15a′ ionization, and (c) similar comparison for 2a″ ionization with the origin set 0.21 eV higher as suggested by the difference in the 15a′ and 2a″ BTE binding energies. The harmonic frequencies in the simulations shown in (b) and (c) have been scaled by factors of 1.17 and 0.90, respectively. The principal vibrational excitations are marked.

For the 15a′ orbital, the predicted vibrational structure [Fig. 5(b)] is dominated by a progression in the ν_{15}^{+} mode, with a much weaker progression involving excitation of the ν_{15}^{+} mode in combination with a single quantum of the ν_{12}^{+} mode. The simulated spectrum for the 2a″ orbital [Fig. 5(c)] predicts that the principal vibrational transitions are due to two progressions, each involving excitation of the ν_{5}^{+} mode, with one of the progressions having an additional single quantum of the ν_{10}^{+} mode. These modes are illustrated in Fig. S3 (supplementary material).

The overall agreement between the FC simulations and experiment is at best modest. Although both simulations would seem to have the ability to rationalize the distinct coarse vibrational structure on the low binding energy side of the experimental band, discrepancies increase beyond the band maximum at ~10.3 eV. While, in principle, fast dissociation can lead to increased diffuseness in photoelectron bands, the loss of the coarse ~0.1 eV spaced vibrational structure observed here would imply dissociation lifetimes of just a few fs. Without further evidence we therefore discount this mechanism as a full explanation.

Significantly, the overall width of the predicted 2a″ FC vibrational envelope clearly exceeds that of the second photoelectron band observed in the binding energy range 9.8–11.4 eV (Fig. 5). Hence, even if a simple overlap of the 15a′ and 2a″ vibrational structures with an empirically adjusted offset is anticipated, the experimental bandwidth and loss of structure to high binding energy cannot be reproduced. In fact, confidence in these FC simulation results is further eroded because the harmonic scaling factors required to induce the apparent agreement with the experimental progression are, respectively, 1.17 and 0.9. Both of these scaling factors fall well beyond the typical B3LYP harmonic frequency scaling of ~0.97 required to correct for well-documented limitations of the harmonic model.[75] Hence, we conclude that, unlike the $X\,^2A''$ state photoelectron band, the harmonic FC simulations here fail to provide a fully convincing model to explain the experimental observations. Going further, we may infer the likelihood of strong vibronic interaction between the $A\,^2A'$ and $B\,^2A''$ states from this behavior and its implied invalidation of the underlying FC assumption of nuclear dynamics on a single adiabatic potential surface. Vibronic interactions of a similar nature have recently been investigated in *cis*- and *trans*-dichloroethene.[76–78]

In the third photoelectron band, the BTEs for the vertical binding energies (Table II) suggest that the main contribution to the low binding energy region should be due to the 14a′ orbital. In the experimental spectrum of this band (Fig. 6), weak vibrational structure is observed in the binding energy range ~13.2 to 14.2 eV. Our FC simulation for the 14a′ orbital ionization appears qualitatively to replicate such structure appearing on the leading edge of the experimental band, and to suggest a plausible width for this band (although experimentally that is obscured by developing overlap with the next three transitions whose binding energies are indicated by the BTE values marked in Fig. 6).

Published under an exclusive license by AIP Publishing

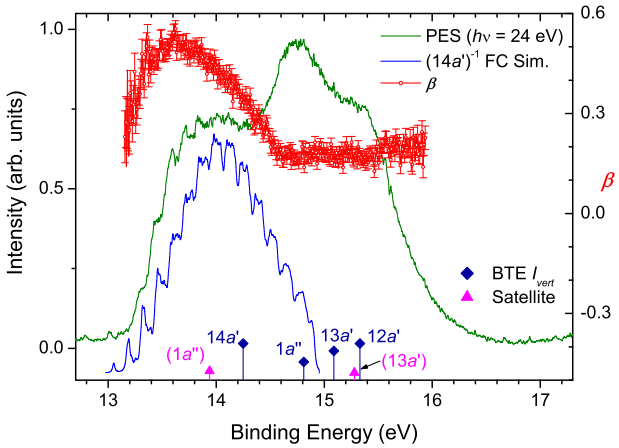

FIG. 6. The third band of the magic angle photoelectron spectrum of imidazole, recorded with a photon energy of 24 eV, and the β-parameter measurement across this region. The BTE vertical ionization energies are marked at the bottom, along with the (1a″) and (13a′) satellite transitions. A TD-B3LYP/cc-pVDZ FC simulation for the lowest 14a′ ionization, with harmonic frequencies scaled by a factor 1.2, is included for comparison.

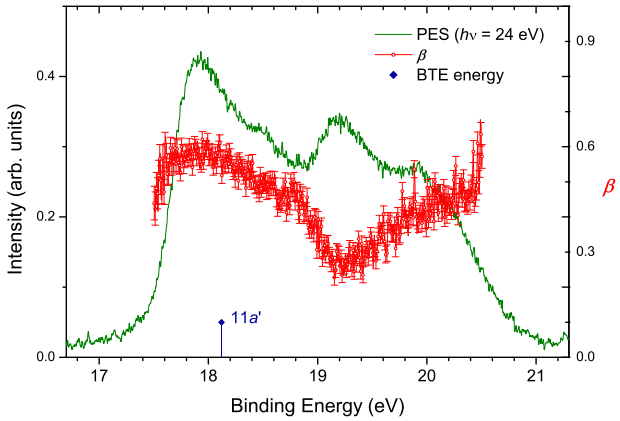

FIG. 7. The fourth band of the magic angle photoelectron spectrum of imidazole, recorded with a photon energy of 24 eV, and the β-parameter measurement across this region. No vibrational simulations were attempted for this region (see the text).

According to the FC simulation for the 14a′ orbital, progressions involving various combinations of the ν_{13}^+ and ν_{14}^+ modes, and, to a lesser extent, the ν_{10}^+ mode, form the major features in the simulated spectrum. The experimental spacings between the vibrational peaks are somewhat irregular, but near the beginning of the band the separation is ~145 meV. The calculated harmonic vibrational energies of the ν_{13}^+ and ν_{14}^+ modes are ~20% lower than this experimental value (see Fig. S3 of the supplementary material), and without such an unexpectedly large scaling, as applied in Fig. 6, the FC simulation provides only a qualitative model for the vibrational structure observed in the third photoelectron band. It should be borne in mind, however, that a $2h$-$1p$ satellite of ^{2}A″ symmetry, associated with the 1a″ orbital, is predicted at 13.94 eV and, hence, will influence the profile of the third photoelectron band at low binding energies.

The final photoelectron peak(s) in the binding energy range 17–21 eV is shown in Fig. 7. Unlike the lower energy peaks, it has no clear vibrational structuring, and consequently no FC simulations have been attempted.

D. Photoelectron branching ratios

The photoionization dynamics for the eight outermost occupied orbitals of imidazole (3a″ through to 11a′) have been studied theoretically using CMS–Xα calculations. The dipole matrix elements obtained in these calculations can be further processed to generate partial (orbital specific) cross sections and β-parameters. The former are shown plotted in Fig. S4 (supplementary material), but these cannot be directly compared with the experiment as absolute cross sections were not obtained. Relative cross sections (intensities) can, however, be compared as electronic state branching ratios. In the present case, this comparison is further restricted since only the first photoelectron band (associated with the $X\ ^2$A″ state) is due to ionization out of a single orbital (3a″).

The experimental branching ratio for a specific photoelectron band, or group of bands, is defined as the intensity in that band divided by the sum of the intensities in all the energetically accessible bands. Thus, at each photon energy, the experimental branching ratios sum to unity. The theoretical branching ratios are similarly defined in terms of the calculated photoionization partial cross sections, normalized by the combined total cross section. Therefore, the theoretical branching ratios must also sum to unity at a given photon energy.

We compare the experimental branching ratios for the first, second, and third photoelectron bands with the corresponding summed 3a″, (15a′ + 2a″), and (1a″, 14a′, 13a′, 12a′) partial channel cross section ratios. The resulting branching ratios are presented in Fig. 8, where experiment and theory are seen to be in good accord over the full photon energy range.

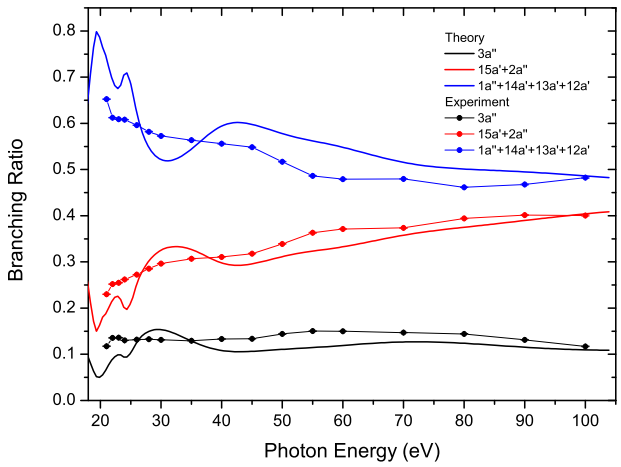

FIG. 8. The experimental and theoretical intensity branching ratios for the first, second, and third photoelectron bands, corresponding to the 3a″, (15a′ + 2a″), and (1a″, 14a′, 13a′, 12a′) orbitals. The theoretical curves for each band were obtained by summing the CMS-Xα photoionization partial cross sections corresponding to the orbitals assigned to that photoelectron band.

Published under an exclusive license by AIP Publishing

The theoretical branching ratios display rather more structure at the lowest photon energies than is experimentally observed. On closer inspection of the calculations, this structure can be attributed to two strong ka' shape resonances, below ~10 eV electron kinetic energy, which are predicted in the $(a')^{-1}$ photoionization channels. These are especially obvious in the 15a′, 14a′, 13a′ partial cross sections (see Fig. S4), but it is not unexpected for such resonances to be exaggerated in fixed geometry CMS–Xα calculations, such as those performed here.[79]

Despite the limitations inherent in this branching ratio comparison, the overall agreement with the experiment achieved by the CMS–Xα calculations offers some assurance that they can provide meaningful descriptions and predictions for the imidazole photoionization dynamics. In Sec. IV E, we consider the behavior of the photoelectron anisotropy parameters using these calculations.

E. Photoelectron angular distributions

An overview of how the experimental β-parameter varies across the photoelectron bands is available for the spectrum recorded at a photon energy of 24 eV (Fig. 3). Further examples of the magic angle, outer valence photoelectron spectra, and the corresponding β-parameter curves at photon energies of 26, 30, and 50 eV may be found in Figs. S5–S7 (supplementary material). It is clear that the measured β-parameters depend on the specific ionic state and the photon energy, but may also show strong variation across the profile of an individual photoelectron band.

To pursue the photon energy dependences for specific photoelectron bands, vibrationally averaged experimental β-parameters, corresponding with the binding energies specified in Table I, have been extracted. Only region 1 encompasses a photoelectron band due to ionization out of a single orbital (3a″). The binding energy ranges of the other regions have been chosen to correlate with specific structure occurring in the experimental photoelectron spectrum (Fig. 3) and the electron signal within a specific region is not necessarily associated with a single orbital. This mixing may arise from the overlap of a photoelectron band corresponding to a particular orbital with that of an adjacent orbital with a similar ionization energy. The breakdown of the single particle model of ionization,[30] leading to the formation of satellites, may also result in the mixing of contributions from different orbitals. For example, our ADC(3) results predict that region 4 contains, in addition to the main-line associated with the 14a′ orbital, a satellite whose intensity originates from the 1a″(π) orbital. In Table I, we have used our ADC(3) calculations to predict which orbitals may contribute to ionization in a specific energy range and photoelectron band.

Figure 9(a) shows the calculated and experimental energy-dependent β anisotropy parameters associated with the first photoelectron band (unambiguously assigned to the single 3a″ orbital). These are in good agreement and exhibit a photon energy dependence typical of that expected for a π-orbital,[80–82] namely, a rapid rise from a low value near threshold to reach a high plateau value at an electron kinetic energy of ~40 eV.

The variation in the β-parameter with increasing vibrational excitation across the $X\,^2A''$ state photoelectron band profile is shown in Fig. 4. As can be seen, the β-value exhibits some correlations

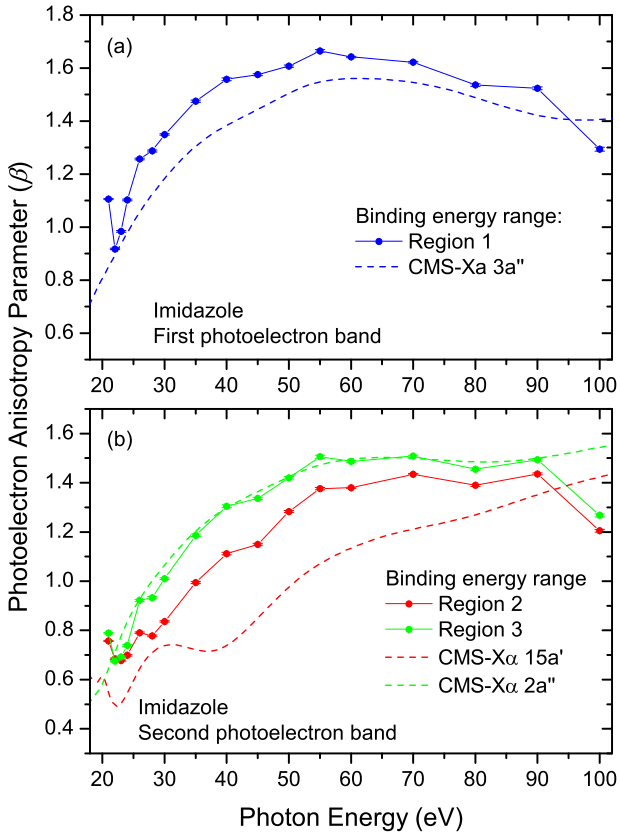

FIG. 9. A comparison between the experimental and theoretically predicted photoelectron anisotropy parameters, β, for (a) the first photoelectron band due to the $(3a'')^{-1}$ $X\,^2A''$ state and (b) the second photoelectron band due to the $(15a')^{-1}$ $A\,^2A'$ and $(2a'')^{-1}$ $B\,^2A''$ states. The binding energy regions used to sample the experimental data are defined in Table I.

with the well-delineated vibrational structure, but the values coinciding with the peaks of the vibrational structure remain essentially constant and do not depend on the level of vibrational excitation (the weak decline in β across the band is readily attributable to the reduction in electron kinetic energy with increasing vibrational excitation at a fixed photon energy—not to any vibrational dynamics). Such a behavior is expected for an orbital where the photoionization can be described within the Born–Oppenheimer approximation of fully decoupled electronic and nuclear motions. This inference is consistent with the good agreement found between the simulated $(3a'')^{-1}$ $X\,^2A''$ state vibrational structure, based on FC factors, and the observed spectrum.

The binding energy ranges for regions 2 and 3 (Table I), which encompass the second photoelectron band (Fig. 3), have been chosen such that region 2 includes all the observed vibrational structure and region 3 covers the featureless higher binding energy range. The calculated photon energy-dependent anisotropy parameters for the 15a′ and 2a″ orbitals are plotted in Fig. 9(b), together with the experimental β-parameters for these regions. A comparison between the theoretical and experimental results shows that for region 3 the

Published under an exclusive license by AIP Publishing

energy dependence of the β-parameter is very similar to that calculated for the 2a″ orbital, suggesting that the energetic ordering is indeed 15a′ < 2a″, as predicted (Table II) by the CC methods. On the other hand, the data for region 2 lie midway between those calculated for the 15a′ and 2a″ orbitals. A likely explanation is that the β values for the 15a′ are indeed lower, but that contributions from the higher 2a″ ionization are not fully excluded by the selected binding energies for region 2.

Figures 3 and 5 show that the β-value across the second photoelectron band starts low near the low binding energy edge and increases toward higher binding energies. At photon energies above 26 eV the β-values clearly reach a plateau in the second half of the band (Figs. S5–S7). The observed low β-value near the beginning of the second photoelectron band, and the higher value reached toward the center of the band, already noted in Fig. 9(b), allows us to infer that the binding energy of the 15a′ orbital is less than that of the 2a″ orbital, in corroboration with our best theoretical estimates of the vertical binding energies of these two orbitals.

The third photoelectron band (Fig. 6) is attributed to ionization from three σ-type orbitals (14a′, 13a′, and 12a′) and one π-type orbital (1a″). According to our ADC(3) results (Table II), the single particle model of ionization[30] is valid for the three σ-type orbitals with each orbital possessing a well-defined main-line. However, the 1a″ main-line pole strength is only ~0.5 and a $2h$-$1p$ shake-down satellite deriving intensity from the 1a″ orbital is predicted near the beginning of the third band. The anisotropy across this binding energy range of 13.1–16.3 eV has been analyzed by dividing the range into four regions (Table I and Fig. 3). Regions 6 and 7 comprise two broad featureless bands. In contrast, vibrational structure is observed in regions 4 and 5. The demarcation between regions 4 and 5 does not correspond to any distinct feature in the experimental spectrum and has been chosen simply to investigate whether the photoionization dynamics differ within the binding energy range 13.1–14.3 eV.

The experimental β-parameters for regions 4–7, and the calculated anisotropy parameters for the 14a′, 13a′, 12a′ and 1a″ orbitals, are plotted in Fig. 10. The experimental β-parameters for regions 4 and 5 are similar, as are those for regions 6 and 7. The calculated β-values for the 12a′, 13a′, and 14a′ orbitals are similar to one another and increase fairly slowly as the photon energy increases. Such an energy dependence is characteristic of ionization out of a σ-type orbital.[80–82] Contrastingly, the calculated β-value for the 1a″ orbital is everywhere larger, and shows a more rapid rate of increase, as would be expected for a π-type orbital.[80–82]

While all the experimental β-values are effectively midway between limits set by the theoretical predictions, suggesting that all the sampled regions may represent some averaging of σ- and π-type orbital ionizations, the observation of the highest β-values in region 4 could indicate a significant contribution from the 1a″ shake-down satellite transition identified by our ADC(3) calculations (Table II) as occurring at 13.78 eV. This satellite would thus fall on the low energy side of the third photoelectron band (Fig. 6). No theoretical β-parameter predictions are available for this satellite, but we may assume that it would be similar to the characteristic π-type β-parameter associated with the 1a″ main-line.

The observed variation in the β-parameter across the third photoelectron band (Fig. 6) provides an alternative view of the photoelectron anisotropy, with a clear distinction between regions

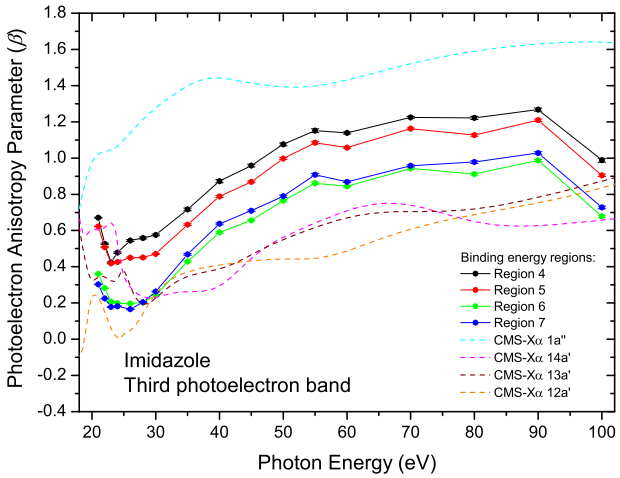

FIG. 10. A comparison between the experimental and theoretically predicted photoelectron anisotropy parameters, β, for ionizations contributing to the third photoelectron band (regions 4–7; see Table I and Fig. 3). The $(14a')^{-1}$ $C\ ^2A'$, $(1a'')^{-1}$ $D\ ^2A''$, $(13a')^{-1}$ $E\ ^2A'$, and $(12a')^{-1}$ $F\ ^2A'$ states lie in these regions (Table II); see the text for details.

4 and 5, and regions 6 and 7. The initial rise, and subsequent fall, of β in regions 4 and 5 suggests that the intensity near the beginning of the third band arises predominantly from the 1a″ orbital, but that contributions from σ-type orbitals increase toward higher binding energy. The contribution from the 1a″ main-line transition is, however, somewhat harder to identify. Nevertheless, the variation in the measured β-parameter appears to support the prediction from the ADC(3) calculations of a low energy $2h$-$1p$ satellite of π-character.

The fourth photoelectron band (Fig. 7), appearing in the binding energy range 17.3–21.0 eV, arises from the 11a′, 10a′, and 9a′ orbitals, but our calculations predict (Table II) that only the 11a′ orbital possesses a main-line, and even in this case, the pole strength is only ~0.58. Clusters of satellites due to the 11a′ orbital, and especially the 10a′ and 9a′ orbitals, form a broad band in the theoretical ADC(3) photoelectron spectrum (Fig. 2). To analyze the experimental spectrum (Fig. 7) formed by these satellites, four binding energy ranges have been defined, and these correspond to regions 8–11 (Table I and Fig. 3). The latter two regions correspond to bands centered at binding energies of ~19.2 and 19.9 eV, while the broad band at lower binding energy is further subdivided into two regions, 8 and 9, in response to the weak shoulder visible at ~18.4 eV in Fig. 7. Figure 11 shows the experimental β-parameters for regions 8–11, and the calculated anisotropy parameters for the 11a′ and 10a′ orbitals. The experimental β-parameter for region 10 is noticeably lower than those for regions 8, 9, and 11 near threshold (Figs. 3 and 7). As the photon energy increases, the β-parameters for the four regions become similar and exhibit an energy dependence typically associated with ionization out of a σ-type orbital (see Figs. S5–S7 of the supplementary material). The calculated β-parameter for the 10a′ orbital is significantly lower than that for the 11a′ orbital near threshold, perhaps suggesting that satellite states with significant contribution from the $(10a')^{-1}$ configuration contribute to the intensity in region 10.

Published under an exclusive license by AIP Publishing

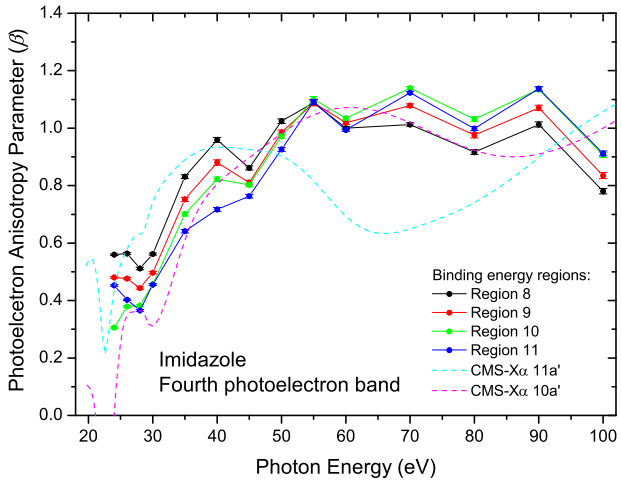

FIG. 11. A comparison between the experimental and theoretically predicted photoelectron anisotropy parameters, β, for ionizations contributing to the fourth photoelectron band (regions 8–11; see Table I and Fig. 3). CMS-Xα results are shown for the 11a′ and 10a′ orbitals.

V. CONCLUSIONS

We have studied the valence photoelectron spectrum of room temperature imidazole vapor at high resolution using a wide range of photon energies, extending up to 100 eV. In the outer valence region, we have further examined the photoelectron angular distribution, employing pairs of spectra recorded with linearly polarized radiation oriented perpendicular and parallel to the electron detector axis to extract the anisotropy parameter, β. The experiments are complemented by theoretical calculations aiming to identify the electronic and vibrational excitations and to provide photoionization cross sections and β-parameters.

ADC(3) calculations have been used to estimate the vertical ionization transition energies; going beyond the independent electron ($1h$) model, these cover various final states with $2h$-$1p$ and mixed $1h/2h$-$1p$ character. Such calculations are essential for interpreting the inner valence region, but in fact they identify the possibility of intense $2h$-$1p$ satellites of the $(1a'')^{-1}$ and $(13a')^{-1}$ ionizations at energies as low as 13.8 and 15.3 eV, respectively, in the outer valence region of the spectrum. Conversely, and with these exceptions, the outer valence photoelectron bands observed below a binding energy of ~18 eV are confirmed as direct single electron orbital ionizations, and this region has then received the more intensive examination.

Various other theoretical methods treating electron correlation and orbital relaxation have been used to estimate vertical ionization energies. Coupled cluster calculations have been extrapolated to the complete basis limit to provide a set of best theoretical estimates, which are used to provisionally assign the structure observed in the outer valence photoelectron spectrum. Nevertheless, possible ambiguities due to the close similarity of the 15a′ and 2a″ binding energies and the predicted presence of the 1a″ and 13a′ satellites in this outer valence region remain to be settled. The intensity profile of the second band in the experimental spectra, which is assigned to the $(15a')^{-1}$ $A\ ^2A'$ and $(2a'')^{-1}$ $B\ ^2A''$ states, is not sufficient to distinguish these two contributions. The third major structure in the spectrum is more complex with three peaks that appear to correspond to overlapping bands but is predicted to encompass four main-line transitions and two satellites according to the calculated binding energies.

The measurement of the photoelectron angular distribution provides partial corroboration and clarification of the assignments. In the second photoelectron band, low values of the anisotropy parameter, β, are recorded on the low binding energy side of the band, but these rise to a higher, sustained value by the band center. From this, the energetic ordering 15a′ < 2a″ can be inferred, based on the general characteristics of σ- and π-orbital angular distributions and, more specifically, on the theoretically predicted β-values for these states obtained in the current study. Likewise, the β-value is significantly higher in the photoelectron band around 13.8 eV (regions 4 and 5) than it is in the adjacent bands around 14.8 and 15.4 eV (regions 6 and 7), again taken as indicative of a strong π-type contribution to the former that may be associated with the predicted 1a″ satellite at 14 eV binding energy. Nevertheless, a clear contribution of the 1a″ main-line excitation remains undetermined by this analysis.

A central aim of this study has been to establish how far the vibronic structure deviates from a simple adiabatic model. The $X\ ^2A''$ state photoelectron band exemplifies this level of isolated electronic state approximation. Its distinct vibrational peaks have spacings that are essentially (with only minor scaling) reproduced by harmonic vibrational calculation, and intensities that are in excellent agreement with the calculated harmonic Franck–Condon factors. This has facilitated a full vibrational assignment. Moreover, the β-value variation correlates closely with the vibrational features and, for a given photon excitation energy, the value of β at the vibrational peak positions is effectively constant across the X state band, confirming the decoupling of electronic and vibrational motion implicit in the Franck–Condon model.

The low binding energy region of the second photoelectron band, provisionally associated above with the 15a′ ionization, also displays vibrational structure, appearing as a simple progression superimposed on a broader base of unresolved transitions. A Franck–Condon simulation with modified harmonic frequencies semi-quantitatively reproduces the first few vibrational peaks. Correspondingly, the 2a″ Franck–Condon simulation can be caused to match the continuation of the experimental "progression," but again only after modification of the calculated harmonic frequencies, and it fails to rationalize the loss of distinct vibrational structure observed on the high binding energy side of the band. Most tellingly, its overall vibrational envelope extends well beyond the experimental width of the second photoelectron band. It is thus concluded that this band cannot be modeled as a simple overlapping superposition of two independent vibrational progressions related to ionization out of the 15a′ and 2a″ orbitals. The required up- and down-scaling of the calculated harmonic frequencies indicates that curvature of both the upper and lower adiabatic potentials may be considered in some way deficient. We therefore hypothesize a vibronic coupling between these two close lying $(15a')^{-1}$ and $(2a'')^{-1}$ states, with the nuclear dynamics occurring over the coupled potentials of both states.

This does not necessarily invalidate the interpretation of the change in β-parameter noted across the second photoelectron band.

Published under an exclusive license by AIP Publishing

Theoretically, it can be expected that when the dynamics are formed by two interacting states, the observed asymmetry will be determined by the leading term in the state expansion.[83] This has been observed, for example, in the photoelectron band system due to the $A\ ^2B_2$, $B\ ^2A_1$, and $C\ ^2A_2$ states of *cis*-dichloroethene[76] with the vibronic interaction confirmed by *ab initio* calculation.[77]

The structure observed in the photoelectron band of imidazole around 14 eV can be qualitatively reproduced by Franck–Condon simulation for the 14a′ ionization (albeit with, again, a surprisingly large rescaling of the calculated harmonic frequencies), but this rather contradicts the β-parameter measurement for this band, which has been interpreted as indicating a significant π-type character, putatively from the 1a″ satellite. In fact, however, the β-parameter varies strongly across the band, which might result from either the blending together of two or more overlapping, non-interacting state ionizations or from β displaying a non-Franck–Condon dependence on the degree of vibrational excitation. This again raises the possibility of vibronic coupling between at least some of the adjacent ionic states ($C\ ^2A'$, $D\ ^2A''$, $E\ ^2A''$, and $F\ ^2A'$) associated with the third photoelectron band.

Recent studies on *cis*- and *trans*-dichloroethene[76–78] have investigated the influence of non-adiabatic nuclear dynamics in the outer valence ionic states. In particular, the theoretical modeling predicted vibronic interactions between the $A\ ^2B_2$, $B\ ^2A_1$, and $C\ ^2A_2$ states, and the $D\ ^2B_1$ and $E\ ^2B_2$ states, leading to complex photoelectron band systems. Moreover, the experimental anisotropy parameters, measured across a particular band system, exhibited a highly irregular dependence upon the level of vibrational excitation. Such an energy dependence is at odds with expectations based on the adiabatic approximation of isolated electronic states, each having an associated (non-interacting) potential energy surface. The similarity between some of the present results for imidazole, and those for dichloroethene, suggest that vibronic coupling may be affecting the valence ionic states of imidazole. An *ab initio* investigation of the possible vibronic coupling in imidazole is ongoing.

SUPPLEMENTARY MATERIAL

See the supplementary material for the presentation of additional experimental spectra, tables of computed geometry and vibrational modes, and a table giving cation vibrational energies.

ACKNOWLEDGMENTS

D.M.P.H. acknowledges the Science and Technology Facilities Council (United Kingdom) for financial support. S.T.P. was supported by the U.S. Department of Energy, Office of Science, Office of Basic Energy Sciences, Division of Chemical Sciences, Geosciences, and Biosciences, under Contract No. DE-AC02-06CH11357. A.B.T., E.V.G., E.K.G., and A.D.S. acknowledge Grant No. FZZE-2020-0025 from the Ministry of Science and Higher Education of the Russian Federation. A.D.S. also acknowledges the Russian Foundation for Basic Research for the support under Project No. 19-03-00947. M.P. acknowledges the Academy of Finland for financial support. A.R.A. acknowledges the Horizon 2020 program I4Future for financial support (Grant Agreement No. 713606). The University of Nottingham High Performance Computing Facility provided computational resources partially supporting this investigation. The authors acknowledge MAX IV Laboratory for time on Beamline FinEstBeAMS under Proposal No. 20190182. Research conducted at MAX IV, a Swedish National User Facility, was supported by the Swedish Research Council under Contract No. 2018-07152, the Swedish Governmental Agency for Innovation Systems under Contract No. 2018-04969, and Formas under Contract No. 2019-02496. They thank the technical staff for their support and for the smooth operation of the facility.

DATA AVAILABILITY

Raw data were generated at the MAXIV synchrotron radiation facility. Derived data supporting the findings of this study are available from the corresponding author upon reasonable request.

REFERENCES

[1] M. N. R. Ashfold, B. Cronin, A. L. Devine, R. N. Dixon, and M. G. D. Nix, Science **312**, 1637 (2006).
[2] A. L. Devine, B. Cronin, M. G. D. Nix, and M. N. R. Ashfold, J. Chem. Phys. **125**, 184302 (2006).
[3] D. J. Hadden, K. L. Wells, G. M. Roberts, L. T. Bergendahl, M. J. Paterson, and V. G. Stavros, Phys. Chem. Chem. Phys. **13**, 10342 (2011).
[4] H. Yu, N. L. Evans, V. G. Stavros, and S. Ullrich, Phys. Chem. Chem. Phys. **14**, 6266 (2012).
[5] W. Arbelo-González, R. Crespo-Otero, and M. Barbatti, J. Chem. Theory Comput. **12**, 5037 (2016).
[6] S. Cradock, R. H. Findlay, and M. H. Palmer, Tetrahedron **29**, 2173 (1973).
[7] L. Klasinc, B. Ruščić, F. Kajfež, and V. Šunjić, Int. J. Quantum Chem. **14**(S5), 367 (1978).
[8] B. G. Ramsey, J. Org. Chem. **44**, 2093 (1979).
[9] A. B. Trofimov, D. M. P. Holland, I. Powis, R. C. Menzies, A. W. Potts, L. Karlsson, E. V. Gromov, I. L. Badsyuk, and J. Schirmer, J. Chem. Phys. **146**, 244307 (2017).
[10] D. M. P. Holland, I. Powis, A. B. Trofimov, R. C. Menzies, A. W. Potts, L. Karlsson, I. L. Badsyuk, T. E. Moskovskaya, E. V. Gromov, and J. Schirmer, J. Chem. Phys. **147**, 164307 (2017).
[11] W. von Niessen, J. Schirmer, and L. S. Cederbaum, Comput. Phys. Rep. **1**, 57 (1984).
[12] V. G. Zakrzewski and W. von Niessen, J. Comput. Chem. **14**, 13 (1993).
[13] V. G. Zakrzewski and J. V. Ortiz, Int. J. Quantum Chem. **52**, 23 (1994).
[14] H. Sekino and R. J. Bartlett, Int. J. Quantum Chem. **26**, 255 (1984).
[15] J. Geertsen, M. Rittby, and R. J. Bartlett, Chem. Phys. Lett. **164**, 57 (1995).
[16] J. F. Stanton and J. Gauss, J. Chem. Phys. **103**, 1064 (1995).
[17] M. Nooijen and J. G. Snijders, J. Chem. Phys. **102**, 1681 (1995).
[18] A. I. Krylov, Annu. Rev. Phys. Chem. **59**, 433 (2008).
[19] O. Christiansen, H. Koch, and P. Jørgensen, J. Chem. Phys. **103**, 7429 (1995).
[20] H. Koch, H. J. A. Jensen, P. Jørgensen, and T. Helgaker, J. Chem. Phys. **93**, 3345 (1990).
[21] H. Koch and P. Jørgensen, J. Chem. Phys. **93**, 3333 (1990).
[22] E. Dalgaard and H. J. Monkhorst, Phys. Rev. A **28**, 1217 (1983).
[23] J. Schirmer, A. B. Trofimov, and G. Stelter, J. Chem. Phys. **109**, 4734 (1998).
[24] A. B. Trofimov and J. Schirmer, J. Chem. Phys. **123**, 144115 (2005).
[25] A. L. Dempwolff, A. C. Paul, A. M. Belogolova, A. B. Trofimov, and A. Dreuw, J. Chem. Phys. **152**, 024113 (2020).
[26] A. L. Dempwolff, A. C. Paul, A. M. Belogolova, A. B. Trofimov, and A. Dreuw, J. Chem. Phys. **152**, 024125 (2020).
[27] J. Schirmer, L. S. Cederbaum, and O. Walter, Phys. Rev. A **28**, 1237 (1983).
[28] J. Schirmer and G. Angonoa, J. Chem. Phys. **91**, 1754 (1989).
[29] H. G. Weikert, H. D. Meyer, L. S. Cederbaum, and F. Tarantelli, J. Chem. Phys. **104**, 7122 (1996).
[30] L. S. Cederbaum, W. Domcke, J. Schirmer, and W. von Niessen, Adv. Chem. Phys. **65**, 115 (1986).

Published under an exclusive license by AIP Publishing

[31] D. Dill and J. L. Dehmer, J. Chem. Phys. **61**, 692 (1974).
[32] J. W. Davenport, Ph.D. thesis, University of Pennsylvania, 1976.
[33] M. Born and R. Oppenheimer, Ann. Phys. **389**, 457 (1927).
[34] G. Herzberg, *Molecular Spectra and Molecular Structure III: Electronic Spectra and Electronic Structure of Polyatomic Molecules* (Van Nostrand Reinhold, New York, 1966).
[35] K. Kooser, A. Kivimäki, P. Turunen, R. Pärna, L. Reisberg, M. Kirm, M. Valden, M. Huttula, and E. Kukk, J. Synchrotron Radiat. **27**, 1080 (2020).
[36] R. Pärna, R. Sankari, E. Kukk, E. Nõmmiste, M. Valden, M. Lastusaari, K. Kooser, K. Kokko, M. Hirsimäki, S. Urpelainen, P. Turunen, A. Kivimäki, V. Pankratov, L. Reisberg, F. Hennies, H. Tarawneh, R. Nyholm, and M. Huttula, Nucl. Instrum. Methods Phys. Res., Sect. A **859**, 83 (2017).
[37] S. Sasaki, K. Kakuno, T. Takada, T. Shimada, K. Yanagida, and Y. Miyahara, Nucl. Instrum. Methods Phys. Res., Sect. A **331**, 763 (1993).
[38] R. Follath and F. Senf, Nucl. Instrum. Methods Phys. Res., Sect. A **390**, 388 (1997).
[39] P. Baltzer, L. Karlsson, M. Lundqvist, and B. Wannberg, Rev. Sci. Instrum. **64**, 2179 (1993).
[40] J. Cooper and R. N. Zare, J. Chem. Phys. **48**, 942 (1968).
[41] I. Powis, D. M. P. Holland, E. Antonsson, M. Patanen, C. Nicolas, C. Miron, M. Schneider, D. Y. Soshnikov, A. Dreuw, and A. B. Trofimov, J. Chem. Phys. **143**, 144304 (2015).
[42] D. M. P. Holland, S. Nandi, C. Nicolas, J. D. Bozek, M. Patanen, and I. Powis, Chem. Phys. **542**, 111050 (2021).
[43] J. E. Reutt, L. S. Wang, Y. T. Lee, and D. A. Shirley, J. Chem. Phys. **85**, 6928 (1986).
[44] D. M. P. Holland, A. C. Parr, D. L. Ederer, J. L. Dehmer, and J. B. West, Nucl. Instrum. Methods Phys. Res., Sect. A **195**, 331 (1982).
[45] S. H. Southworth, A. C. Parr, J. E. Hardis, J. L. Dehmer, and D. M. P. Holland, Nucl. Instrum. Methods Phys. Res., Sect. A **246**, 782 (1986).
[46] M. O. Krause, T. A. Carlson, and P. R. Woodruff, Phys. Rev. A **24**, 1374 (1981).
[47] A. Fahlman, M. O. Krause, T. A. Carlson, and A. Svensson, Phys. Rev. A **30**, 812 (1984).
[48] U. Becker, D. Szostak, H. G. Kerkhoff, M. Kupsch, B. Langer, R. Wehlitz, A. Yagishita, and T. Hayaishi, Phys. Rev. A **39**, 3902 (1989).
[49] J. F. Stanton and J. Gauss, J. Chem. Phys. **111**, 8785 (1999).
[50] T. H. Dunning, J. Chem. Phys. **90**, 1007 (1989).
[51] R. A. Kendall, T. H. Dunning, and R. J. Harrison, J. Chem. Phys. **96**, 6796 (1992).
[52] D. Feller, J. Chem. Phys. **96**, 6104 (1992).
[53] D. Feller, J. Chem. Phys. **98**, 7059 (1993).
[54] M. J. Frisch, G. W. Trucks, H. B. Schlegel, G. E. Scuseria, M. A. Robb, J. R. Cheeseman, G. Scalmani, V. Barone, B. Mennucci, G. A. Petersson, H. Nakatsuji, M. Caricato, X. Li, H. P. Hratchian, A. F. Izmaylov, J. Bloino, G. Zheng, J. L. Sonnenberg, M. Hada, M. Ehara, K. Toyota, R. Fukuda, J. Hasegawa, M. Ishida, T. Nakajima, Y. Honda, O. Kitao, H. Nakai, T. Vreven, J. A. Montgomery, Jr., J. E. Peralta, F. Ogliaro, M. Bearpark, J. J. Heyd, E. Brothers, K. N. Kudin, V. N. Staroverov, T. Keith, R. Kobayashi, J. Normand, K. Raghavachari, A. Rendell, J. C. Burant, S. S. Iyengar, J. Tomasi, M. Cossi, N. Rega, J. M. Millam, M. Klene, J. E. Knox, J. B. Cross, V. Bakken, C. Adamo, J. Jaramillo, R. Gomperts, R. E. Stratmann, O. Yazyev, A. J. Austin, R. Cammi, C. Pomelli, J. W. Ochterski, R. L. Martin, K. Morokuma, V. G. Zakrzewski, G. A. Voth, P. Salvador, J. J. Dannenberg, S. Dapprich, A. D. Daniels, O. Farkas, J. B. Foresman, J. V. Ortiz, J. Cioslowski, and D. J. Fox, Gaussian 09, Revision C.01, Gaussian, Inc., Wallingford, CT, 2010.
[55] CFOUR, Coupled cluster techniques for Computational Chemistry, a quantum-chemical program package by J. F. Stanton, J. Gauss, M. E. Harding, and P. G. Szalay, with contributions from A. A. Auer, R. J. Bartlett, U. Benedikt, C. Berger, D. E. Bernholdt, Y. J. Bomble, L. Cheng, O. Christiansen, M. Heckert, O. Heun, C. Huber, T.-C. Jagau, D. Jonsson, J. Jusélius, K. Klein, W. J. Lauderdale, D. A. Matthews, T. Metzroth, L. A. Mück, D. P. O'Neill, D. R. Price, E. Prochnow, C. Puzzarini, K. Ruud, F. Schiffmann, W. Schwalbach, C. Simmons, S. Stopkowicz, A. Tajti, J. Vázquez, F. Wang, and J. D. Watts and the integral packages MOLECULE (J. Almlöf and P. R. Taylor), PROPS (P. R. Taylor), ABACUS (T. Helgaker, H. J. A. Jensen, P. Jørgensen, and J. Olsen), and ECP routines by A. V. Mitin and C. van Wüllen, for the current version, see http://www.cfour.de.
[56] Y. Shao, Z. Gan, E. Epifanovsky, A. T. B. Gilbert, M. Wormit, J. Kussmann, A. W. Lange, A. Behn, J. Deng, X. Feng, D. Ghosh, M. Goldey, P. R. Horn, L. D. Jacobson, I. Kaliman, R. Z. Khaliullin, T. Kuś, A. Landau, J. Liu, E. I. Proynov, Y. M. Rhee, R. M. Richard, M. A. Rohrdanz, R. P. Steele, E. J. Sundstrom, H. L. Woodcock, P. M. Zimmerman, D. Zuev, B. Albrecht, E. Alguire, B. Austin, G. J. O. Beran, Y. A. Bernard, E. Berquist, K. Brandhorst, K. B. Bravaya, S. T. Brown, D. Casanova, C.-M. Chang, Y. Chen, S. H. Chien, K. D. Closser, D. L. Crittenden, M. Diedenhofen, R. A. DiStasio, H. Do, A. D. Dutoi, R. G. Edgar, S. Fatehi, L. Fusti-Molnar, A. Ghysels, A. Golubeva-Zadorozhnaya, J. Gomes, M. W. D. Hanson-Heine, P. H. P. Harbach, A. W. Hauser, E. G. Hohenstein, Z. C. Holden, T.-C. Jagau, H. Ji, B. Kaduk, K. Khistyaev, J. Kim, J. Kim, R. A. King, P. Klunzinger, D. Kosenkov, T. Kowalczyk, C. M. Krauter, K. U. Lao, A. D. Laurent, K. V. Lawler, S. V. Levchenko, C. Y. Lin, F. Liu, E. Livshits, R. C. Lochan, A. Luenser, P. Manohar, S. F. Manzer, S.-P. Mao, N. Mardirossian, A. V. Marenich, S. A. Maurer, N. J. Mayhall, E. Neuscamman, C. M. Oana, R. Olivares-Amaya, D. P. O'Neill, J. A. Parkhill, T. M. Perrine, R. Peverati, A. Prociuk, D. R. Rehn, E. Rosta, N. J. Russ, S. M. Sharada, S. Sharma, D. W. Small, A. Sodt, T. Stein, D. Stück, Y.-C. Su, A. J. W. Thom, T. Tsuchimochi, V. Vanovschi, L. Vogt, O. Vydrov, T. Wang, M. A. Watson, J. Wenzel, A. White, C. F. Williams, J. Yang, S. Yeganeh, S. R. Yost, Z.-Q. You, I. Y. Zhang, X. Zhang, Y. Zhao, B. R. Brooks, G. K. L. Chan, D. M. Chipman, C. J. Cramer, W. A. Goddard, M. S. Gordon, W. J. Hehre, A. Klamt, H. F. Schaefer, M. W. Schmidt, C. D. Sherrill, D. G. Truhlar, A. Warshel, X. Xu, A. Aspuru-Guzik, R. Baer, A. T. Bell, N. A. Besley, J.-D. Chai, A. Dreuw, B. D. Dunietz, T. R. Furlani, S. R. Gwaltney, C.-P. Hsu, Y. Jung, J. Kong, D. S. Lambrecht, W. Liang, C. Ochsenfeld, V. A. Rassolov, L. V. Slipchenko, J. E. Subotnik, T. Van Voorhis, J. M. Herbert, A. I. Krylov, P. M. W. Gill, and M. Head-Gordon, Mol. Phys. **113**, 184 (2015).
[57] I. Powis, A. B. Trofimov, I. L. Bodzuk, D. M. P. Holland, A. W. Potts, and L. Karlsson, Chem. Phys. **415**, 291 (2013).
[58] A. W. Potts, D. M. P. Holland, I. Powis, L. Karlsson, A. B. Trofimov, and I. L. Bodzuk, Chem. Phys. **415**, 84 (2013).
[59] M. W. Schmidt, K. K. Baldridge, J. A. Boatz, S. T. Elbert, M. S. Gordon, J. H. Jensen, S. Koseki, N. Matsunaga, K. A. Nguyen, S. Su, T. L. Windus, M. Dupuis, and J. A. Montgomery, J. Comput. Chem. **14**, 1347 (1993).
[60] M. S. Gordon and M. W. Schmidtt, in *Theory and Applications of Computational Chemistry*, edited by C. E. Dykstra, G. Frenking, K. S. Kim, and G. E. Scuseria (Elsevier, Amsterdam, 2005), p. 1167.
[61] G. Herzberg, *Molecular Spectra and Molecular Structure II: Infrared and Raman Spectra of Polyatomic Molecules* (Van Nostrand Reinhold, New York, 1945).
[62] M. J. Frisch, G. W. Trucks, H. B. Schlegel, G. E. Scuseria, M. A. Robb, J. R. Cheeseman, G. Scalmani, V. Barone, G. A. Petersson, H. Nakatsuji, X. Li, M. Caricato, A. V. Marenich, J. Bloino, B. G. Janesko, R. Gomperts, B. Mennucci, H. P. Hratchian, J. V. Ortiz, A. F. Izmaylov, J. L. Sonnenberg, D. Williams-Young, F. Ding, F. Lipparini, F. Egidi, J. Goings, B. Peng, A. Petrone, T. Henderson, D. Ranasinghe, V. G. Zakrzewski, J. Gao, N. Rega, G. Zheng, W. Liang, M. Hada, M. Ehara, K. Toyota, R. Fukuda, J. Hasegawa, M. Ishida, T. Nakajima, Y. Honda, O. Kitao, H. Nakai, T. Vreven, K. Throssell, J. J. A. Montgomery, J. E. Peralta, F. Ogliaro, M. Bearpark, J. J. Heyd, E. Brothers, K. N. Kudin, V. N. Staroverov, T. A. Keith, R. Kobayashi, J. Normand, K. Raghavachari, A. Rendell, J. C. Burant, S. S. Iyengar, J. Tomasi, M. Cossi, J. M. Millam, M. Klene, C. Adamo, R. Cammi, J. W. Ochterski, R. L. Martin, K. Morokuma, O. Farkas, J. B. Foresman, and D. J. Fox, Gaussian 16 Revision A.03, Gaussian, Inc., Wallingford, CT, 2016.
[63] P. Downie and I. Powis, J. Chem. Phys. **111**, 4535 (1999).
[64] M. Staniforth, S. Daly, K. L. Reid, and I. Powis, J. Chem. Phys. **139**, 064304 (2013).
[65] J. C. Slater, *The Self-Consistent Field for Molecules and Solids* (McGraw-Hill, New York, 1974).
[66] J. G. Norman, Jr., Mol. Phys. **31**, 1191 (1976).
[67] G. Wendin, "Breakdown of one-electron pictures in photoelectron spectra," in *Breakdown of the One-Electron Pictures in Photoelectron Spectra*, Structure and Bonding Vol. 45 (Springer, Berlin, 1982).
[68] A. B. Trofimov, J. Schirmer, D. M. P. Holland, L. Karlsson, R. Maripuu, K. Siegbahn, and A. W. Potts, Chem. Phys. **263**, 167 (2001).
[69] A. W. Potts, A. B. Trofimov, J. Schirmer, D. M. P. Holland, and L. Karlsson, Chem. Phys. **271**, 337 (2001).

Published under an exclusive license by AIP Publishing

[70] A. B. Trofimov, J. Schirmer, D. M. P. Holland, A. W. Potts, L. Karlsson, R. Maripuu, and K. Siegbahn, J. Phys. B: At. Mol. Phys. **35**, 5051 (2002).
[71] I. L. Zaytseva, A. B. Trofimov, J. Schirmer, O. Plekan, V. Feyer, R. Richter, M. Coreno, and K. C. Prince, J. Phys. Chem. A **113**, 15142 (2009).
[72] H. Koch, O. Christiansen, P. Jørgensen, and J. Olsen, Chem. Phys. Lett. **244**, 75 (1995).
[73] O. Christiansen, H. Koch, P. Jørgensen, and J. Olsen, Chem. Phys. Lett. **256**, 185 (1996).
[74] H. Larsen, K. Hald, J. Olsen, and P. Jørgensen, J. Chem. Phys. **115**, 3015 (2001).
[75] J. P. Merrick, D. Moran, and L. Radom, J. Phys. Chem. A **111**, 11683 (2007).
[76] I. Powis, R. C. Menzies, D. M. P. Holland, A. B. Trofimov, A. D. Skitnevskaya, E. V. Gromov, E. Antonsson, M. Patanen, C. Nicolas, and C. Miron, J. Chem. Phys. **149**, 074305 (2018).
[77] A. B. Trofimov, I. Powis, R. C. Menzies, D. M. P. Holland, E. Antonsson, M. Patanen, C. Nicolas, C. Miron, A. D. Skitnevskaya, E. V. Gromov, and H. Köppel, J. Chem. Phys. **149**, 074306 (2018).
[78] A. T. Duran, I. Powis, D. M. P. Holland, C. Nicolas, J. Bozek, A. B. Trofimov, E. K. Grigoricheva, and A. D. Skitnevskaya, J. Chem. Phys. **154**, 094303 (2021).
[79] J. L. Dehmer, D. Dill, and S. Wallace, Phys. Rev. Lett. **43**, 1005 (1979).
[80] D. M. P. Holland, L. Karlsson, and W. von Niessen, J. Electron Spectrosc. Relat. Phenom. **113**, 221 (2001).
[81] D. M. P. Holland, I. Powis, G. Öhrwall, L. Karlsson, and W. von Niessen, Chem. Phys. **326**, 535 (2006).
[82] I. Powis, I. L. Zaytseva, A. B. Trofimov, J. Schirmer, D. M. P. Holland, A. W. Potts, and L. Karlsson, J. Phys. B: At. Mol. Phys. **40**, 2019 (2007).
[83] W. Domcke, Phys. Scr. **19**, 11 (1979).

Published under an exclusive license by AIP Publishing